Journal of Nanobiotechnology

RESEARCH

Open Access

Endogenous electric field coupling Mxene sponge for diabetic wound management: haemostatic, antibacterial, and healing

Hai Zhou[1,2†], Lianglong Chen[1†], Chaoyang Huang[1†], Ziwei Jiang[1], Huihui Zhang[1], Xiaoyang Liu[1], Fengyi Zhu[2], Qiulan Wen[3], Pengwei Shi[4*], Kun Liu[5*] and Lei Yang[2*]

Abstract

Improper management of diabetic wound effusion and disruption of the endogenous electric field can lead to passive healing of damaged tissue, affecting the process of tissue cascade repair. This study developed an extracellular matrix sponge scaffold (K_1P_6@Mxene) by incorporating Mxene into an acellular dermal stroma-hydroxypropyl chitosan interpenetrating network structure. This scaffold is designed to couple with the endogenous electric field and promote precise tissue remodelling in diabetic wounds. The fibrous structure of the sponge closely resembles that of a natural extracellular matrix, providing a conducive microenvironment for cells to adhere grow, and exchange oxygen. Additionally, the inclusion of Mxene enhances antibacterial activity(98.89%) and electrical conductivity within the scaffold. Simultaneously, K_1P_6@Mxene exhibits excellent water absorption (39 times) and porosity (91%). It actively interacts with the endogenous electric field to guide cell migration and growth on the wound surface upon absorbing wound exudate. In in vivo experiments, the K_1P_6@Mxene sponge reduced the inflammatory response in diabetic wounds, increased collagen deposition and arrangement, promoted microvascular regeneration, Facilitate expedited re-epithelialization of wounds, minimize scar formation, and accelerate the healing process of diabetic wounds by 7 days. Therefore, this extracellular matrix sponge scaffold, combined with an endogenous electric field, presents an appealing approach for the comprehensive repair of diabetic wounds.

Keywords Endogenous electric field, Acellular dermal matrix, Hydroxypropyl chitosan, Sponge scaffold, Diabetic wound

†Hai Zhou, Lianglong Chen and Chaoyang Huang contributed equally to this work.

*Correspondence:
Pengwei Shi
shiz_057@163.com
Kun Liu
liukun09@smu.edu.cn
Lei Yang
yuanyang@smu.edu.cn
[1]Department of Burns, Nanfang Hospital, Southern Medical University, Jingxi Street, Baiyun District, Guangdong 510515, PR China
[2]Department of Microscopy and Hand and Foot Surgery, Yunfu People's Hospital, Central Laboratory of YunFu People's Hospital, No. 120 Huanshi East Road, Yuncheng District, Yunfu City 527399, PR China
[3]Department of Orthopaedic Surgery, Nanfang Hospital, Southern Medical University, Guangzhou, Guangdong Province, PR China
[4]Emergency Department, Nanfang Hospital, Southern Medical University, Guangzhou 510515, PR China
[5]Experimental Education/Administration Centre, National Demonstration Centre for Experimental Education of Basic Medical Sciences, Key Laboratory of Functional Proteomics of Guangdong Province, Department of Cell Biology, School of Basic Medical Sciences, Southern Medical University, Guangzhou 510515, PR China

Introduction

Conventional wound healing is a complex, well-coordinated process involving a series of cellular and biochemical reactions, typically categorised into haemostasis and inflammation, hyperplasia, and scar remodelling stages [1]. However, diabetes can induce microvascular disease and abnormal microcirculation, compromising blood flow and nutrient delivery to the wound area, which delays wound healing due to insufficient oxygen and nutrient delivery [2, 3]. Additionally, diabetes impairs immune function, increasing patients' susceptibility to wound infections [4]. The hyperglycaemic state leads to the formation of advanced glycation end products (AGEs) that alter collagen function and structure, further disrupting normal tissue repair processes and delaying wound healing [5]. Diabetes-induced chronic hyperglycaemia often perpetuates a state of chronic inflammation, characterized by sustained elevation of pro-inflammatory cytokines and reduced neovascularization, both of which impede normal cellular function and tissue repair [6]. As early diabetic wounds progress to chronic refractory wounds, standard dressings on the market become ineffective [7], often leaving surgery or amputation as the last resort for treatment [8]. Currently, emerging strategies for diabetes management emphasise early detection, intervention, and prevention [9]. It is hypothesised that timely and comprehensive management of the wound healing process upon the initial presentation of wounds in diabetic patients may prevent acute wounds from evolving into chronic, hard-to-heal chronic wounds.

Wound-induced endogenous electric fields (EFs) play a crucial role in guiding cell migration and promoting tissue repair [10]. In 1890, Du Bois-Reymond discovered that injured fingers exhibited electrical activity compared with uninjured ones, suggesting a connection between electric currents and wound healing [11]. Zhao M. et al. reported that the skin spontaneously generates an endogenous electric field with an intensity between 5 and 100 $\mu A/cm^2$ after injury [12]. The mechanism involves the transport of cations (mainly Na^+) from epidermal cells to the basal layer of the skin tissue through ion channels and pumps, while anions (Cl^-) are transported to the epidermal layer. The accumulation of cations in the basal layer and anions in the top layer creates and sustains the transdermal potential (TEP) at the injury site [13]. The flow of ions within and between cells is the primary driver of the endogenous electric field. Inhibition of this electric field impairs the skin repair process. To expedite tissue regeneration, researchers have developed functional electrodes that simulate the natural EF at wound sites, applying external electrical stimulation (ES) to promote the migration of macrophages, neutrophils, and keratinocytes, thus accelerating wound healing. Despite its efficacy, external ES is limited by the complexity of the procedure, which involves assessing current-related parameters, wound status, patient tolerance, and other factors. Moreover, electrotherapy devices tend to be large and cumbersome [14]. Therefore, finding effective and practical ways to use EF to promote chronic wound healing remains a pressing challenge.

Diabetic wound repair is often complicated by infections, which can disrupt the healing process and potentially lead to systemic infections or even amputations [15]. While numerous antibiotics have been developed to combat bacterial infections, their overuse has spurred the emergence of antibiotic-resistant strains, posing significant therapeutic hurdles [16]. In response to this issue, research has increasingly focused on natural antimicrobial nanomaterials [4]. Mxene, a promising two-dimensional (2D) transition metal carbide, exhibits unique structural properties that make it particularly suitable for biomedical applications [17]. Its high conductivity facilitates efficient separation and migration of photogenerated charge carriers, while its large surface area, high hydrophilicity, and good biocompatibility further enhance its appeal [18]. Notably, Mxene exhibits robust antibacterial activity through several mechanisms: Mxene nanosheets can electrostatically capture bacteria and disrupt bacterial membranes with their sharp edges [19]. Additionally, Mxene generates reactive oxygen species (ROS) and enables photothermal inactivation of bacteria, further enhancing its antimicrobial efficacy [20]. Combining Mxene with other organic and inorganic materials through mixed crosslinking holds promise for developing advanced biological dressings with electroactive and antibacterial properties, offering novel strategies for diabetic wound management [21].

Hydroxypropyl chitosan (HPCS) not only preserves the alkalinity and electropositivity of chitosan but also weakens both intermolecular and intramolecular hydrogen bonding, thereby enhancing water solubility and reactivity. HPCS effectively strengthens the hydrogen bonds between fibres, with its amino groups forming ionic bonds with the carboxyl groups on the fibre surface. The spongy dressing based on HPCS exhibits a well-connected microporous structure and excellent fluid absorption capacity, which supports intercellular interactions and promotes cell proliferation [22]. Additionally, it offers good air permeability to isolate bacteria and features soft materials to reduce wound damage, among other advantages. However, chitosan sponge on its own has drawbacks, such as low mechanical strength and susceptibility to dissolution in water, which significantly limits its application as a wound dressing.

Porcine acellular dermal matrix (PADM) is produced by removing the epidermal layer and cellular components from porcine skin through physical and chemical processes, leaving behind an extracellular matrix rich in

collagen [23]. PADM offers an optimal environment for the growth and regeneration of host cells, acting as a scaffold for the proliferation of skin fibroblasts. It aids in reconstructing collagen components and promoting the orderly arrangement and distribution of fibroblasts [24]. Moreover, PADM's good plasticity allows it to be blended and cross-linked with other organic and inorganic materials to produce flexible and degradable sponge scaffolds [25]. However, PADM-based sponge scaffolds lack antibacterial properties and have poor mechanical strength, making them prone to collapse under external pressure and susceptible to swelling and disintegration when exposed to water. Therefore, blending or cross-linking PADM with other biological materials is essential to enhance its functionality and improve its physical and chemical properties.

Based on the above findings, this study developed a Mxene sponge scaffold incorporating PADM and HPCS (K_1P_6@Mxene)(Fig. 1). Mxene, known for its bioelectrical signal conduction, antibacterial, and anti-inflammatory properties, was integrated into the three-dimensional network structure of porcine acellular dermal matrix and chitosan through physical crosslinking. These materials were combined to form a loose, porous sponge scaffold via homogeneous dispersion, freeze-drying, and cross-linking. The resulting dressing possesses multiple

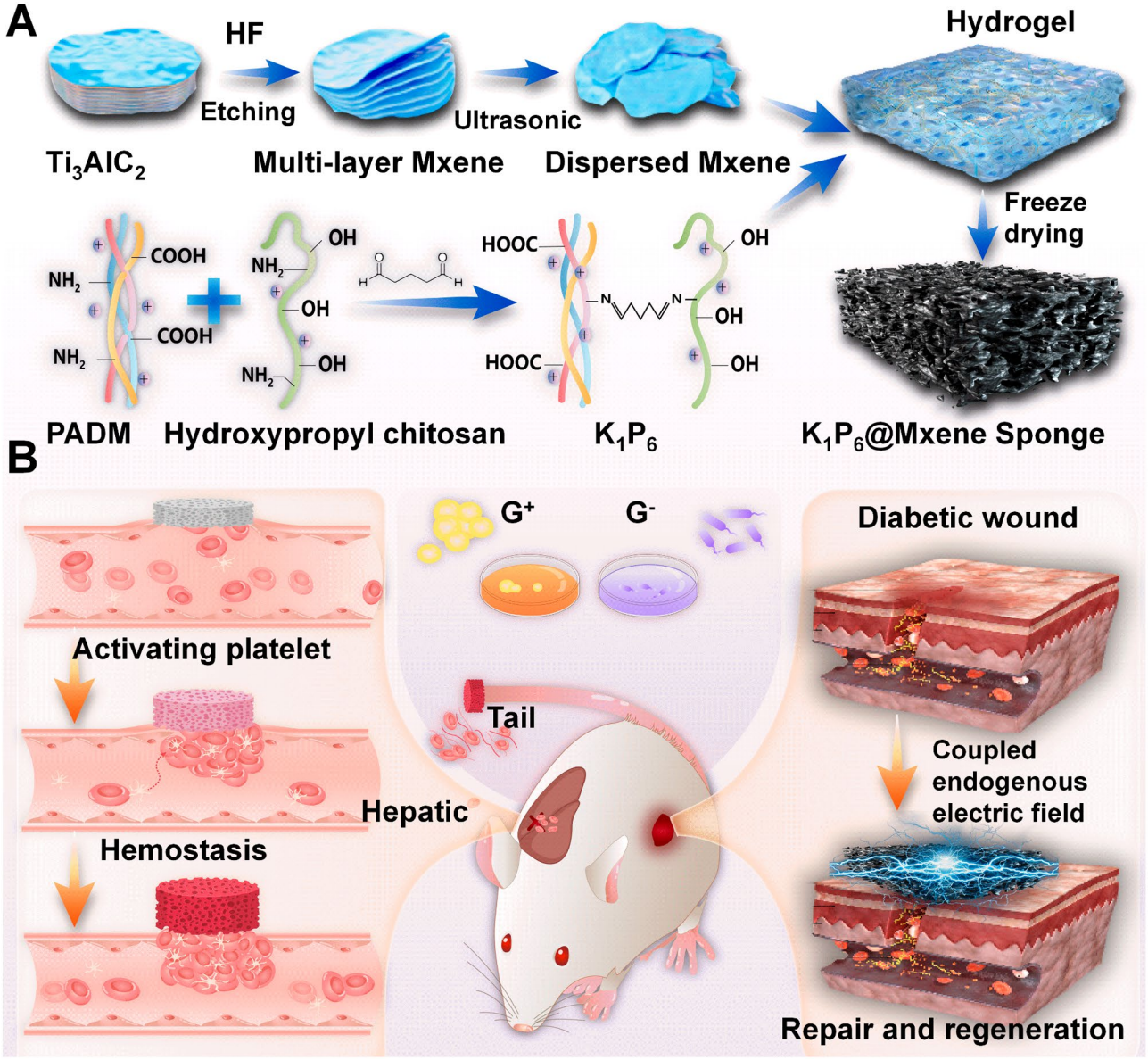

Fig. 1 Fabrication and application of Mxene-based antibacterial haemostatic sponge with endogenous electric field coupling. (**A**) Schematic illustration of the fabrication process for the K_1P_6@Mxene sponge; (**B**) Application of the K_1P_6@Mxene sponge for haemostasis and diabetic wound healing

functions, including haemostatic, anti-inflammatory, and antibacterial properties. It promotes the proliferation and migration of wound repair-related cells and enhances collagen secretion by coupling with the wound's endogenous electric field. This stimulates granulation tissue formation and revascularisation, and accelerates the healing of diabetic wounds. The novel scaffold provides a promising approach for repairing diabetic skin damage and preventing acute wounds from progressing into chronic refractory wounds.

Materials and methods

Materials

Ti_3AlC_2 (purity: 99.7%) was purchased from Foshan Xinxi Technology Co., Ltd. Hydroxypropyl chitosan, 25% glutaraldehyde solution, and 40% hydrofluoric acid were obtained from Macklin Reagent Co., Ltd. (Shanghai, China). The Collagen Sponge (CS) was procured from Shanghai Qisheng Biologics Co., Ltd. Unless otherwise specified, other chemicals or reagents were sourced from Sigma-Aldrich. The human umbilical vein endothelial cells (HUVECs) and L929 cells were purchased from the Clinical Research Centre of Nanfang Hospital, Southern Medical University. *Escherichia coli* and *Staphylococcus aureus* were obtained from the Guangzhou Institute of Microbiology. Male SD rats (10 weeks old) were purchased from Zhuhai Bestest Biotechnology Co., Ltd. White Tibetan miniature pigs (six months old, weighing approximately 30 kg) were sourced from Guangzhou Huateng Biotechnology Co., Ltd. The animal experiment protocol was approved by Nanfang Hospital, Southern Medical University (IACUC-LAC-20230822-002). All animal feeding and experiments were conducted following the requirements of the Animal Ethics Committee.

Preparation and characterisation of Mxene

A mixture of 20 mL of 40% HF and 15 mL of deionised water was added to a 100 mL polytetrafluoroethylene reactor. Subsequently, 2 g of Ti_3AlC_2 was weighed and gradually added incrementally into the reactor. The reactor speed was set to 500 rpm, and the reaction was carried out at 40 ℃ for 12 h. After the reaction, the mixture was centrifuged six times at 5000 rpm for 5 min each, until the pH of the supernatant was greater than 6. The centrifugation was then stopped, and the supernatant was discarded. Next, 25 mL of dimethyl sulfoxide (DMSO), the intercalation agent, was added to the residue and stirred at room temperature for 12 h. The mixture was then transferred to a centrifuge tube and centrifuged three times to remove the DMSO. The precipitate was filtered using a 0.22-micron liquid membrane, drained, and placed in a vacuum oven at 40 ℃ for 2 h to obtain accordion-like Mxene.

X-ray photoelectron spectroscopy (XPS, Thermo Scientific™, ESCALAB™ 250Xi, Thermo Fisher Scientific, United States) was used to analyse the surface elements of Mxene and their different valence states. The crystal structure of Mxene was examined using an X-ray diffractometer (XRD, SmartLab SE, Rigaku, Japan). The surface morphology of Mxene was observed with a scanning electron microscope (SEM, Regulus 8100, Hitachi, Japan). The structure of Mxene was further investigated using a transmission electron microscope (TEM, Tecnai G2 F20, FEI, United States). The particle size of Mxene was measured with a particle size analyser (Zetasizer Nano ZS90, Malvern Panalytical, England).

Preparation of porcine acellular dermal matrix-hydroxypropyl chitosan sponge scaffold loading Mxene

The porcine acellular dermal matrix (PADM) powder in deionised water using a homogeniser. Hydroxypropyl chitosan was then added to the PADM solution in varying solute ratios, maintaining the solute concentration of the mixed system at 3%. Subsequently, Mxene powder was incorporated into the mixture at different mass ratios. After thorough homogenisation, the mixture was freeze-dried to form a sponge. The sponge was soaked in a crosslinking agent (a solution of 25% glutaraldehyde in anhydrous ethanol at a volume ratio of 1:5) for 20 min, thoroughly rinsed with deionised water, and freeze-dried again. The final product was labelled based on the mass ratio of Mxene added (0.8%), resulting in the designation of 0.8% Mxene.

Characterisation of materials

Photographs of the prepared sponge samples were taken in both wet and dry states. The surface morphology of the sponges was observed using scanning electron microscopy (SEM, Regulus 8100/8200 Hitachi, Japan). Changes in chemical groups were analysed with a Fourier-transform infrared spectrometer (Nicolet™ iS50 FTIR Spectrometer, Thermo Fisher Scientific, United States). The water absorption, density, and porosity of the sponges were measured using a porous material porosity tester (JHY-120 C). The hydrophilicity of the sponges was determined with a contact angle meter/tensiometer (Theta Flex, Biolin Scientific, Finland). Changes in the mass of the samples with temperature or over time in an oxygen environment were measured using a thermogravimetric analysis/differential scanning calorimetry instrument (TGA/DSC 3+, Mettler Toledo Switzerland). The resistivity of the wet sponges soaked in deionised water was measured with a four-probe resistance-microcurrent tester (Suzhou JinGe, ST2643), and the conductivity was calculated. Conductivity was further observed by connecting the sponge material to both ends of a conductive diode (LED) circuit.

Additionally, cylindrical sponge samples (diameter 12 mm, height 6 mm) were prepared and soaked in double-distilled water (ddH_2O) for 2 h, after which their wet weight (W) was measured. The samples were then placed in a cell incubator at 37 ℃ for three consecutive days, with the damp weight recorded as W_1, W_2, and W_3 on days 1, 2, and 3, respectively. The sponge water retention rate was calculated as W_1/W_n.

In accordance with GB/T1040-2006, an electronic universal testing machine (DR-603 A) was used to cyclically compress both dry and wet sponges for 15 cycles, with each compression reaching a deformation of 60% at a rate of 10 mm/min. The corresponding curves were obtained, and the compression modulus was calculated. Additionally, the sponge samples were shaped into dry cylinders with a diameter of 12 mm and a height of 14 mm. Deionised water was introduced to the sponge, and identical pressure was applied; the morphology of the sample before, during, and after compression was documented and photographed.

To assess the moisture permeability of the material, the water vapour transmittance (WVTR) was determined according to ASTM standards. In brief, a 2 mm thick disc-shaped sample of the material was placed over the mouth of a cylindrical cup containing distilled water and sealed along the edge with a sealing film. The assembly was then incubated at 37 ℃ and 50% relative humidity. The WVTR is calculated using the formula: $WVTR=\Delta W / (A \times T)$, where ΔW represents the mass change of the cup per unit time in grams (g); A denotes the effective area of the sample being measured in square meters (m^2); and T stands for time in days (24 h). All samples were tested three times ($n=3$).

Cell proliferation experiment

A circular sponge sample, 14 mm in diameter and 2 mm in thickness, was sterilised by immersion in a 75% ethanol solution for 6 h. The sponge was then thoroughly rinsed with sterile PBS. The prepared sponge sample was placed in a 12-well plate, and 4 mL of DMEM complete medium (MEM+10% fetal bovine serum+1% penicillin-streptomycin) was added as the solvent. The sponge material was incubated in a cell incubator at 37 ℃ for 24 h to obtain the extract. The cytotoxicity of different material extracts to human umbilical vein endothelial cells (HUVECs) and mouse fibroblasts (L929 cells) was assessed using the cell counting kit-8 (CCK-8) method. The cells were seeded in 96-well plates at a density of 3000 cells per well. After cell adhesion, the media were replaced with extracts from each material group, with the control group using a high-glucose medium. At 24 and 60 h post-medium replacement, the culture medium was discarded, and 100 μL of serum-free DMEM medium and 10 μL of CCK-8 working solution were added to each well. The culture plates were then incubated in a CO_2 incubator at 37 ℃ for 1 h. Subsequently, 100 μL of the reaction liquid from each well was transferred to an unused 96-well plate, and the absorbance value at 450 nm was measured using a multifunctional microplate reader.

Live/dead cell staining

HUVECs and L929 cells in good growth condition were seeded into 24-well plates at a density of 2×10^4 cells per well. Once the cells had adhered and extended, the culture medium was replaced with extracts from the CS, K_1P_6, and K_1P_6@Mxene, while the control group received a high-glucose complete medium. After co-culturing for 72 h, the cells were gently washed with PBS, and 200 μL of prepared live/dead cell staining solution was added to each well. The plates were then incubated in the dark for 30 min before observation under a fluorescence microscope.

Cell adhesion experiment

Sterile sponges (K_1P_6 and K_1P_6@Mxene) were soaked in a high-glucose medium for one hour. HUVECs were then inoculated onto the sponges at a density of 3×10^4 cells per material. After three days of culture, HUVECs were washed with PBS, fixed with 4% paraformaldehyde for 24 h, and rinsed 3 times with PBS to remove any residual paraformaldehyde from the material's surface. Next, 0.1% Triton X-100 was added, and the samples were incubated for 20 min. Finally, the cytoskeleton and nuclei were stained by adding 200 μL of FITC-phalloidin and DAPI mixed staining solution. After incubation at 37 °C for 30 min in darkness, the reaction solution was discarded. 500 μL of serum-free DMEM medium was then added, and the adhesion and spreading behaviour of the cells on different sponges were observed using laser scanning confocal microscopy (LSCM).

Cell migration experiment

HUVECs cultured to the logarithmic growth phase were digested and prepared into cell suspensions at a concentration of 2×10^5 cells/mL. These suspensions were inoculated into 12-well plates and allowed to reach confluence. Once confluence was achieved, two parallel scratch lines were created using a 200 μL pipette tip, followed by two washes with PBS buffer to remove cellular debris. Then, 4 mL of basic medium containing 1% serum was slowly added into the orifice plate. Sponge discs (12 mm in diameter and 2 mm in thickness) were then placed in the Transewell chamber and transferred to an incubator for culture. Microscopic images were captured at various time points to monitor and document cell migration.

Antibacterial performance test

The antibacterial activity of the sponge scaffold was evaluated using *Escherichia coli* (ATCC 25922, a Gram-negative strain) and *Staphylococcus aureus* (ATCC 6538, a Gram-positive strain). The sponge was prepared into disc samples (8 mm in diameter, 1 mm in thickness). Under sterile conditions, 2 mL of a bacterial solution containing 10^7 CFU/mL was applied to the sponge, ensuring thorough impregnation for complete interaction with the bacteria. The samples were incubated at 37 ℃ for 36 h. After incubation, 200 uL of the bacterial solution was collected and placed in a 4-mL centrifuge tube. The solution was diluted to 4 mL with 3.8 mL of Luria Bertani (LB) broth, and further incubated in an oscillating incubator at 37 ℃. At 0, 2, 4, 6, 8, and 10 h, 200 uL of the bacterial suspension was sampled from each tube and transferred to a 96-well plate. The optical density (OD) at 600 nm was measured using a microplate absorbance reader. This test was repeated three times for each group, with a control group that did not include a sponge.

Additionally, under sterile conditions, 2 mL of the bacterial solution with a concentration of 10^7 CFU/mL was applied to the sponge, ensuring full impregnation for complete interaction with the bacteria. The samples were incubated at 37 ℃ for 36 h, followed by gradient dilution of the bacterial solution. A 100 μL aliquot of the diluted bacterial solution was evenly spread on an agar plate and cultured at 37 ℃ for 24 h for colony counting. The control group consisted of a tissue culture plate (TCP) inoculated with bacteria. This test was also repeated three times for each group.

Haemolysis rate test

The blood compatibility of the sponges was evaluated by measuring the haemolysis rate. Citrated pig whole blood was collected (whole blood to 3.8% sodium citrate ratio = 9:1), and 1 mL of this blood was diluted with 9 mL of PBS. A sample suspension was prepared by immersing 5 mg of sponge in 100 μL of normal saline, and 100 μL of this suspension was incubated with 1 mL of diluted blood at 37 ℃ for 4 h. After incubation, the supernatant was collected by centrifugation at 3000 rpm for 10 min, and the OD value of the supernatant at 545 nm was measured using a microplate reader (Varioskan LUX, Thermo Scientific). In this experiment, PBS served as the negative control group, Triton X-100 as the positive control group, and the suspension mass fraction of the red blood cells added was 0.5%. The haemolysis rate (B) was calculated using the following formula: $B = (OD_{sam} - OD_{neg}) / (OD_{pos} - OD_{neg})$. Where B is the haemolysis rate of the material, OD_{sam} is the absorbance of the sample at 545 nm, OD_{neg} is the absorbance of the negative control group at 545 nm, and OD_{pos} is the absorbance of the positive control group at 545 nm.

Determination of in vitro coagulation time

Pig whole blood was collected using a sodium citrate anticoagulant tube. To each 5-mL centrifuge tube, 2 mL of the collected whole blood was added along with a 50 mg sponge sample. Simultaneously, 60 μL of 0.2 mol/L $CaCl_2$ solution was introduced. The mixture of blood and material was then thoroughly mixed, and the time taken for the blood to stop flowing was recorded as the blood coagulation time. This process was repeated three times for each group, and the mean value was calculated. The blank control group did not include any haemostatic material.

Blood clotting index (BCI) test

The sample sponge was cut into 3 mg pieces and placed into a centrifuge tube. Then, 100 uL of pig whole blood was added to the sponge's surface, followed by adding 10 uL of 0.2 mol/L $CaCl_2$ solution. The timing started at this point. After incubating at 37 ℃ for 2 min, 10 mL of deionised water was added to the centrifuge tube to lyse the non-coagulated blood cells, with the incubation continuing at 37 ℃ for an additional 3 min. After this period, the supernatant was collected, and its absorbance at 540 nm was measured using a microplate reader. The blood clotting index (BCI) was calculated using the formula: $BCI\ (\%) = OD_{sample} / OD_{control} \times 100\%$.

Determination of whole blood coagulation dynamics

The whole blood coagulation dynamics of the haemostatic materials were evaluated by measuring the blood clotting index (BCI) at various time points. Pig whole blood was collected using sodium citrate anticoagulant collection tubes, and 2 mL of 0.1 mol/L $CaCl_2$ solution was added to 20 mL of anticoagulated blood to activate it. Immediately, 150 μL of the activated blood was added to the sponge sample. At each designated time point, 3 mL of deionised water was added to the material, and the mixture was incubated at 37 ℃ for 10 min to lyse the non-thrombotic red blood cells through hyperosmosis. Then, 200 μL of the incubated solution was transferred to a 96-well plate, and the absorbance of haemoglobin was measured at 540 nm. The procedure was repeated three times, and the mean value was calculated. Additionally, the pH value of the blood after 24 h was measured, and photographs of the thrombi formed in each group after 24 h of swelling were taken.

Blood cell adhesion test

Discs of collagen sponge (CS), K_1P_6, and K_1P_6@Mxene samples, each with a diameter of 12 mm and a thickness of 1 mm, were prepared. These discs were uniformly placed at the bottom of each well in a 24-well plate and immersed in PBS at 37 ℃ for 1 h. Subsequently, 1 mL of anticoagulated pig whole blood was added to each well

and incubated at 37 ℃ for 5 min. Following this, 1 mL of platelet-rich plasma (PRP) was added to each well and incubated at 37 ℃ for 2 h. After incubation, each sample was washed three times with saline to remove non-adhering red blood cells and platelets. The samples were then fixed by adding 2 mL of 2.5% (v/v) glutaraldehyde and incubated at 37 ℃ for 2 h. After fixation, the samples were rinsed with normal saline three times, dehydrated with gradient alcohol for 15 min, and freeze-dried using tert-butanol instead of ethanol. The prepared specimens were coated with gold, examined using a scanning electron microscope (SEM), and photographed.

SD rat liver injury haemostasis experiment

The haemostatic efficacy of the sponge samples was assessed using an SD rat liver injury model. Male SD rats (weighing 220–250 g) were randomly allocated into three groups: collagen sponge (CS), K_1P_6, and K_1P_6@Mxene. The rats were anaesthetised with 2% pentobarbital sodium and secured on a surgical plate. An abdominal incision was made to expose the liver, and the serous fluid around the liver was carefully removed. A bleeding spot approximately 5 mm in diameter and 3 mm in depth was created on the liver using a scalpel. Sponge samples were then applied to the bleeding area, and observations were recorded every 10 s until the bleeding stopped completely. The haemostatic material was weighed, and the bleeding time was calculated. The experiment was repeated three times for each group.

Rat tail-cutting haemostasis experiment

Male SD rats weighing 220–250 g were anaesthetised with 2% pentobarbital sodium. A scalpel was used to amputate the rat's tail at 50% of its length, and the tail was exposed to air for 15 s to allow for average blood loss. The rats were then randomly assigned to three groups: collagen sponge (CS), K_1P_6, and K_1P_6@Mxene. Haemostatic sponges were applied to the bleeding sites until haemostasis was achieved. The blood absorption capacity of the sponges was assessed, and the bleeding time was recorded. Each experiment was repeated three times for each group.

Rat diabetic wound repair experiment

Ten-week-old healthy male SD rats, each weighing approximately 250±10 g, were used for the study. The animals were sourced from Zhuhai Bestest Biotechnology Co., Ltd. All animal experiments adhered to the guidelines and regulations of the China Experimental Animal Research Ethics Committee. After a week of acclimatisation in the animal house, the SD rats were fasted for 12 h. Type I diabetes was induced via an intraperitoneal injection of 1% streptozotocin (STZ) solution at a dose of 65 mg/kg. Successful induction of diabetes was confirmed by symptoms such as polydipsia, polyphagia, and polyuria, along with random blood glucose levels exceeding 16.7 mM one week post-injection. The diabetic rats were randomly assigned to the control group, Collagen sponge (CS) group, K_1P_6 group, and K_1P_6@Mxene group. The rats were anesthetised with an intraperitoneal injection of 2% pentobarbital sodium. The back of each rat was shaved and disinfected with iodine before creating a full-thickness skin defect (to the deep fascia layer) with a diameter of 12 mm using a hole punch. The sponge sample was applied to the defective wound, with no additional material added to the control group. Finally, sterile gauze and bandages were utilized to secure the dressing and prevent it from detaching. Wound healing was monitored and recorded with a digital camera at various time points post-surgery. If the sponge materials became detached, they were promptly replaced. The wound healing rate was calculated based on the recorded images. The experiment was repeated three times for each group.

Histomorphological analysis

After the surgical procedure, wound tissue samples from rats were collected at designated time points. These samples were fixed using a paraformaldehyde tissue fixation solution and subsequently embedded in paraffin for sectioning. The histomorphological analysis included the assessment of wound inflammation, collagen deposition, angiogenesis, and scarring. This was performed using H&E staining, Masson trichrome staining, and immunohistochemical staining (IL-10, TNF-α, Col I, CD31, and α-SMA).

Statistical analysis

Results are expressed as the mean±standard deviation. Statistical significance among groups was determined using a one-way analysis of variance (ANOVA). Significance levels are indicated as follows: $^{*}p<0.05$, $^{**}p<0.01$, $^{***}p<0.001$, and $^{****}p<0.0001$.

Results and discussion

Preparation and characterisation of hydroxypropyl chitosan-acellular dermal matrix sponge

In this study, the preparation of hydroxypropyl chitosan-acellular dermal matrix sponge was prepared through a series of steps, including dissolution, homogeneous dispersion, freeze-drying, and cross-linking, as illustrated in Fig. 2A. A 3% hydroxypropyl chitosan (HPCS) solution was mixed with a 2.5% porcine acellular dermal matrix (PADM) solution in various volume ratios (Fig. 2B). Increasing the volume ratio of the PADM solution enhanced the sponge's ability to retain its shape after water absorption. Specifically, the water absorption rate of the sponge peaked at a PADM to HPCS volume ratio of 1:6, leading to the selection of the K_1P_6 sponges

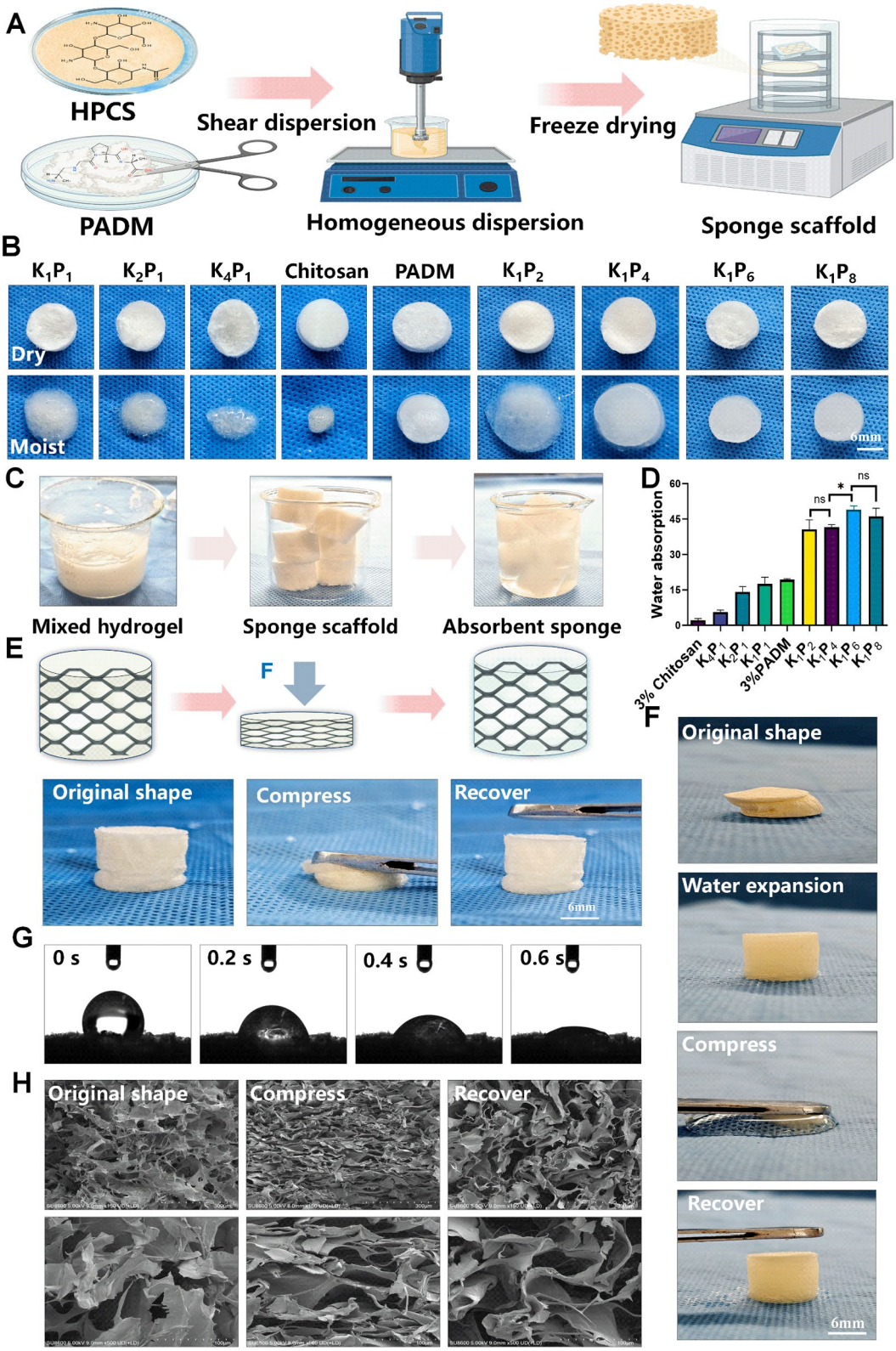

Fig. 2 Preparation and characterisation of hydroxypropyl chitosan-acellular dermal matrix sponge. (**A**) Schematic diagram of composite sponge synthesis; (**B**) Images of the morphology of dry and wet hydroxypropyl chitosan-acellular dermal matrix sponges at varying mix ratios; (**C**) Photographs of mixed hydrogel and sponge scaffold after water absorption; (**D**) Water absorption; (**E**) Photographs of the dry sponge demonstrating shape recovery performance; (**F**) Photographs of the compressed wet sponge demonstrating shape recovery performance; (**G**) Photographs of water droplets on the surface of a dry sponge that is compressed and fixed over time; (**H**) Microstructure of uncompressed and compressed dry sponges

for further experiments (Fig. 2D). Figure 2C illustrates the sponge in its freeze-dried state, which expands and absorbs water upon rehydration. The K_1P_6 sponge exhibits excellent water absorption and swelling characteristics. Due to homogeneous shear and dispersion during preparation, the fibre fragments within the sponge form a large interconnected pore structure and a robust cross-linked network. This configuration allows the sponge to be repeatedly compressed and restored to its shape both in the dry state (Fig. 2E) or after water absorption. The sponge's hydrophilic properties were assessed using a static water contact angle test [26]. As shown in Fig. 2G, the sponge displays superhydrophilic behaviour, with water droplets being absorbed within 0.6 s without leaving residue on the surface. Even partial contact with water results in rapid expansion and swelling at the contact point, highlighting the sponge's strong shape recovery tendency (Fig. 2F). This enhanced hydrophilicity can be attributed to changes in the surface microstructure, where the compressed sponge forms a capillary structure through the densely packed pore walls, aiding in rapid water absorption (Fig. 2H).

Preparation and characterisation of Ti3C2Tx (Mxene)

In this study, hydrofluoric acid (HF) was used as the etching agent to selectively remove the weak and easily hydrolysed Al-C structural units in the titanium-aluminium carbide (Ti_3AlC_2) to obtain multi-layer Mxene materials (Fig. 3A). SEM images reveal that the Mxene obtained through HF etching presents a multi-layer accordion-like structure composed of two-dimensional single-layer lamellar structures due to the strong interaction force between the lamellar layers (Fig. 3B). TEM images further depict the interconnected layers of Mxene with reduced layer spacing, consistent with the observed accordion-like morphology (Fig. 3C). The X-ray diffraction (XRD) pattern of the multi-layer Mxene is illustrated in Fig. 3F. After HF etching, the prominent peak of Ti_3AlC_2 at 39° disappeared, confirming the successful etching of the Al layer [27]. Moreover, the peaks at 9.5° and 19.4° of Ti_3AlC_2 widened and shifted to 8.8° and 18.5°, respectively, indicating the successful conversion of Ti_3AlC_2 to Mxene and partial substitution of Al element by -OH or -F groups. As shown in Fig. 3E, Mxene mainly comprises carbon (C), titanium (Ti), and fluorine (F), suggesting that HF etching effectively removed the Al layer in Ti_3AlC_2 and introduced fluorine into the Mxene structure. Element mapping further supports these findings, as illustrated in Fig. 3D.

Preparation and characterisation of Mxene composite sponge scaffolds

Mxene was uniformly incorporated into K_1P_6 gel at different mass ratios, followed by freeze-drying to form a sponge. Initially, the K_1P_6 sponge appears white, as shown in Fig. 3G. With the addition of Mxene, the composite sponge gradually darkened, becoming blacker as the Mxene content increased. During freeze-drying, the crystallisation and water evaporation processes result in all sponges forming an interconnected, honeycomb-like porous structure. This structure facilitates the adsorption of red blood cells through a three-dimensional network and promotes platelet aggregation. As shown in **Fig. S1**, both K_1P_6 and Mxene sponges, regardless of Mxene content, demonstrate excellent water-triggered structural stability. Upon water absorption, they rapidly expand into elastic spongy bodies, retaining a stable shape even under repeated firm compression. This sponge structure conforms well to wound contours, providing uniform support and pressure. Once hydrated, the sponge becomes soft, ensuring comfort and reducing patient pain. It is easy to position, remove, and can be tailored to specific needs [28]. Furthermore, as Mxene content increases, more Mxene particles are distributed on the surface and pore wall of the composite sponge, resulting in a rough inner surface (Fig. 3H). This roughness may enhance wound healing and promote tissue regeneration [29]. Fig. S2 illustrates the sponges' rapid water absorption upon immersion, alongside their elasticity and shape retention under rotational forces. The compression mechanics of dry and wet sponges with varying Mxene contents were thoroughly evaluated (Fig. S3A and 3B). The K_1P_6@Mxene sponge exhibited excellent compression recovery after 15 consecutive compressions, with a maximum stress of 12.46 kPa recorded in the first cycle. Increasing Mxene content did not significantly enhance the sponge's compression strength and modulus. This phenomenon may be due to the negatively charged groups on Mxene (e.g., -F) and the physical van der Waals forces and intermolecular hydrogen bonding among the numerous -OH groups and the -O groups on K_1P_6 fibres, which slightly improve mechanical strength but do not cause a substantial change [30]. For assessing stable conductivity necessary for transmitting long-term electrical signals, the sponge's conductivity in a wet state was tested. The results showed that as Mxene content increased, the conductivity of the damp sponge gradually improves (Fig. 3O), indicating that the Mxene sponge can absorb wound exudates and transmit bioelectrical signals in response to diabetic wound endogenous electric fields, thereby guiding proliferation, migration, and differentiation [10]. Furthermore, integrating a wet 0.8% Mxene sponge with a circuit allowed a bright light to be emitted from an LED (Fig. 3I and J).

The high water absorption rate of scaffolds benefits tissue regeneration by effectively draining excess biological fluid from wounds and reducing infection risk. The 0.8% Mxene group sponge exhibited superior water absorption

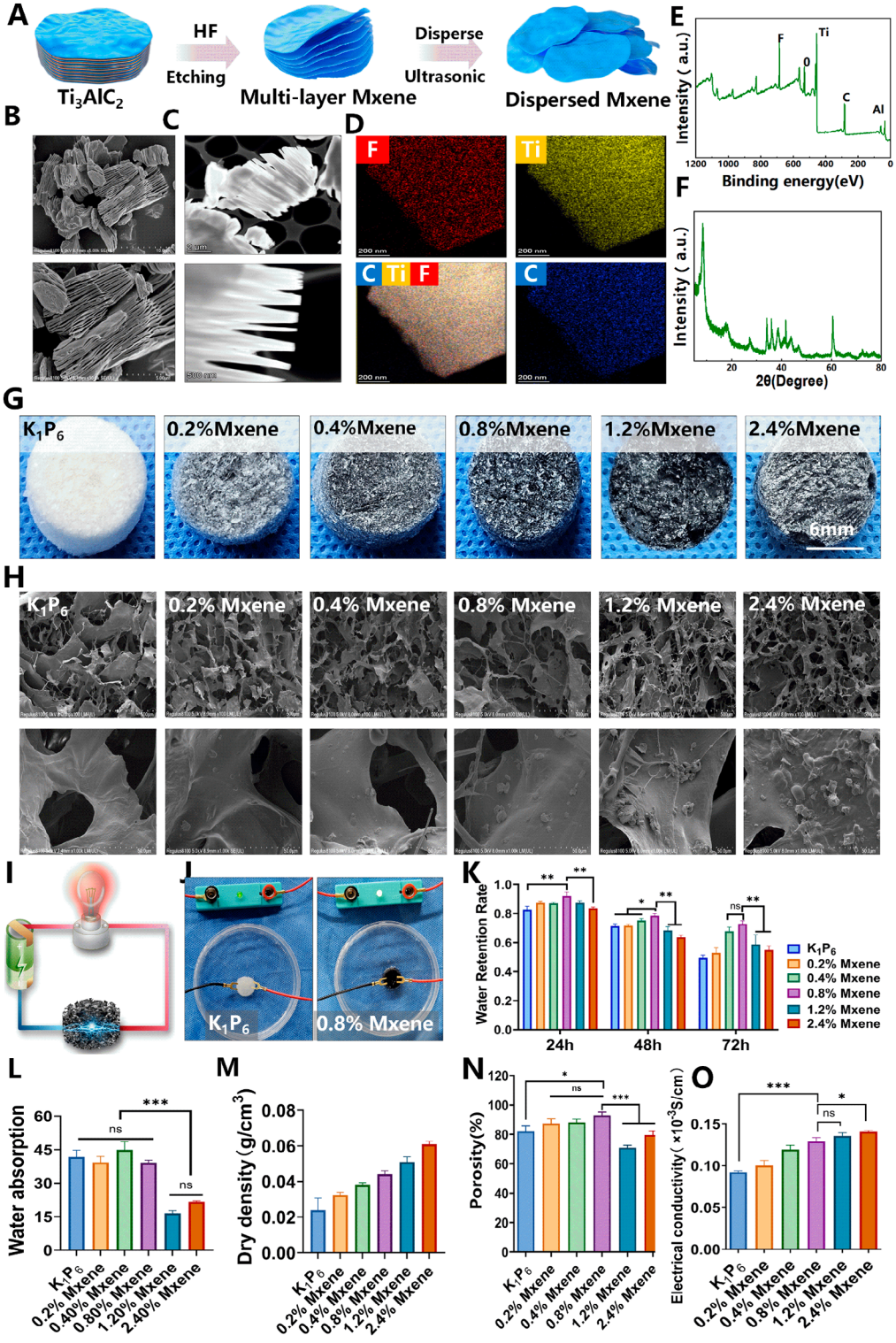

Fig. 3 Preparation and characterisation of Mxene sponge. (**A**) Schematic representation of the Mxene preparation process; (**B**) SEM image; (**C**) TEM image; (**D**) Elemental mapping corresponding to carbon (**C**), fluorine (**F**), and titanium (Ti) in Mxene; (**E**) XPS full spectrum; (**F**) XRD pattern; (**G**) Representative images showing the gross morphology of sponges; (**H**) SEM image; (**I**) Integrated circuit diagram of the sponge structure; (**J**) K_1P_6@Mxene sponge used to illuminate LED in a wet environment; (**K**) Water retention capacity of different sponges; (**L**) Water absorption capacity of the sponges; (**M**) Dry density measurement of sponges; (**N**) Porosity measurement of sponges; (**O**) Wet conductivity measurement of sponges. The data were quantified from three independent experiments and presented as mean ± standard deviation. Statistical analysis was performed using one-way ANOVA followed by Tukey's post-hoc multiple comparison test (*$p < 0.05$, **$p < 0.01$, ***$p < 0.001$)

capacity (39±1.2) compared to the 1.2% and 2.4% Mxene groups, making it more effective at absorbing wound exudates and accommodating blood (Fig. 3L). Moist sponges are more suitable for the human body environment, making it crucial to assess their deformation resistance. The dry density of sponges is depicted in Fig. 3M, with a density of (0.02±0.003) g/cm^3 for the K_1P_6 sponges. Sponge density gradually increases with Mxene content. Fig. S4 displays the water vapour transmission rate, highest for the 0.8% Mxene group at (4231±70.93) g/m^2/24 h, and lowest for the 1.2% Mxene group at (3503.67±96.24) g/m^2/24 h—aligning with porosity and water retention rate results. An optimal water vapour·transfer rate maintains a slightly moist environment for wounds, protecting against bacterial infection. As depicted in Fig. 3K, the water retention rate of the sponge increased with higher Mxene content, peaking at 0.8% Mxene. Further increases in Mxene content led to a gradual decrease in water retention. Additionally, as Mxene content increased, the porosity of each group's sponge increased, with the 0.8% Mxene group reaching the highest porosity at (91±0.2)% (Fig. 3N). This phenomenon can be attributed to three main factors: Firstly, the abundance of hydrophilic hydroxyl groups on the surface of Mxene enhances the hydrophilicity of K_1P_6@Mxene sponge. Secondly, the interpenetrating network formed by hydroxyl and K_1P_6 molecules on the surface of Mxene increases the porosity of the K_1P_6@Mxene sponge, thereby reducing molecular tension at the water-sponge interface and enhancing water affinity [31]. Lastly, hydrogen bonding and ion crosslinking between the Mxene and K_1P_6 system improve the overall structure and physicochemical properties of the K_1P_6@Mxene sponge while enhancing its water-holding performance. However, when Mxene concentration exceeds 0.8% (reaching 1.2%), the excessive hydrophilic effect from surface hydrophilic groups outweighs the relative mass increase of Mxene [32]. It impacts the K_1P_6 structure, reducing porosity and physicochemical properties, consequently decreasing water retention capacity. Water-retaining dressings support skin hydration and maintain a moist healing microenvironment. In conclusion, the 0.8% Mxene exhibits optimal physical and chemical properties and is designated as K_1P_6@Mxene.

Characterisation of composite sponge scaffold K_1P_6@Mxene

We optimised the K_1P_6@Mxene sponge in the initial phase to achieve favourable physical and chemical properties, followed by an elemental analysis of the sponge. As shown in Fig. 4A, elements Ti, C, and N are evenly distributed in K_1P_6@Mxene, indicating that Mxene nanosheets are uniformly integrated within the K_1P_6 sponge. Glutaraldehyde cross-links with amino acid residues in polysaccharides, forming a stable imine structure that enhances the stability and durability of proteins [33].Fourier-transform infrared spectroscopy (FTIR) analysis (Fig. 4B) reveals the stretching vibration of -OH and the bending vibration of -NH_2 in hydroxypropyl chitosan at 3392, 2971, and 1659 cm^{-1}, respectively. The characteristic absorption peaks of PADM appeared at 3277 cm^{-1}, 1628 cm$^{-1,}$ and 1526 cm^{-1}, corresponding to hydrogen bonding between -OH and -NH_2 groups, the amide I band of random coil and helical conformations, and the amide II band of N-H bending vibration, respectively. In the K_1P_6 spectrum, a new imine bond characteristic absorption peak (C=N) was observed at 1620 cm^{-1}. Additionally, the bending vibration of the N-H band of amide II redshifted to 1531 cm^{-1} due to hydrogen bond interaction, and the absorption peak at 3279 cm^{-1} was enhanced, indicating increased hydrogen bond formation. The FTIR spectra of K_1P_6@Mxene closely resemble those of K_1P_6, suggesting two possibilities: (1) no chemical reaction occurs between K_1P_6 and Mxene, with their interaction primarily through van der Waals forces and intermolecular hydrogen bonding between negatively charged surface groups on Mxene (e.g., -OH and -F) and the -OH groups on the K_1P_6 cellulose chain; or (2) the -OH groups on the K_1P_6 chain and Mxene surfaces may undergo hydroxyl condensation with glutaraldehyde, forming a small amount of -C-O-C- bonds similar to the covalent cross-linking within the K_1P_6 chain itself, which may not significantly affect the FTIR pattern of K_1P_6@Mxene [34].

The XRD pattern of the sponge (Fig. 4C) shows that integrating Mxene into the sponge reduces its crystallinity, with the characteristic peak shifting to a lower 2θ angle. Thermogravimetric analysis (TGA) was used to assess the thermal stability of the substance by measuring weight loss with temperature changes [35]. TGA curves (Fig. 4D) indicate three thermal degradation stages between 30 ℃ and 600 ℃ for those 3 sponges. The first stage (30 °C to 250 °C) is associated with the loss of free and bound water, resulting in a mass reduction of approximately 16%. The second stage (250 °C to 400 °C) involves thermal breakdown of the skeleton, with a 42% weight loss, where hydroxyl groups on adjacent molecular chains are removed as water molecules, producing stable intermediates [36]. The final step is the oxidation and decomposition of sponge carbide under heat. K_1P_6@Mxene exhibits a relatively low and broad thermal decomposition temperature. The derivative thermogravimetric (DTG) curve (Fig. 4E) shows that the decomposition peak of K_1P_6 is steeper than that of K_1P_6@Mxene, indicating improved thermal stability due to the addition of Mxene.

To analyse the interaction mechanism between Mxene and K_1P_6, X-ray photoelectron spectroscopy (XPS) was

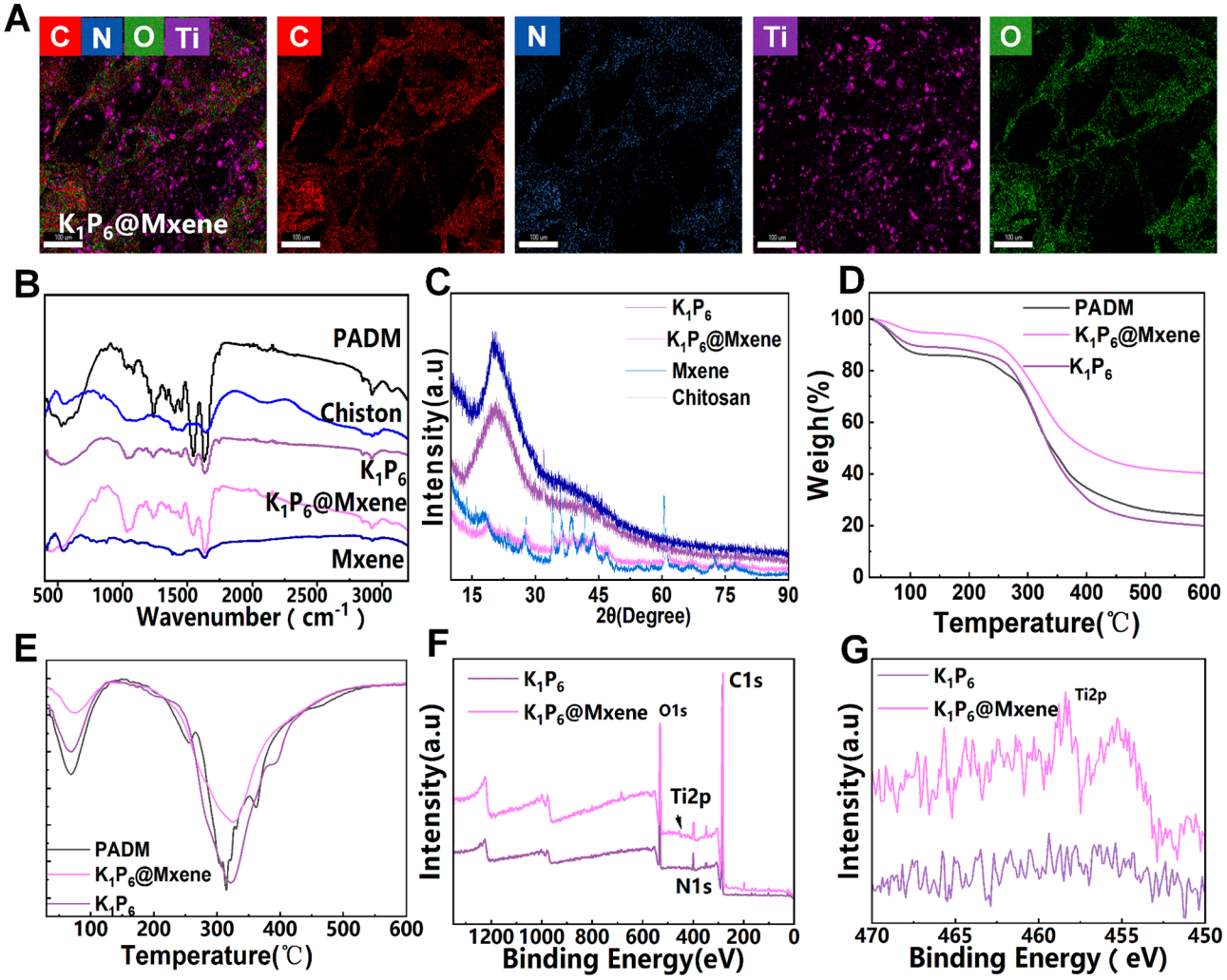

Fig. 4 Physicochemical characteristics of K_1P_6@Mxene sponge scaffold. (**A**) Elemental mapping corresponding to C, N, O, and Ti in K_1P_6@Mxene sponge; (**B**) Fourier transform infrared spectroscopy; (**C**) X-ray diffraction pattern; (**D**) Thermogravimetric analysis curve (TGA); (**E**) Derivative thermogravimetric analysis curve (DTG); (**F**) Full spectrum of X-ray photoelectron spectroscopy (XPS); and (**G**) Ti 2p

employed. The typical XPS peaks for K_1P_6@Mxene and K_1P_6 are shown in Fig. 4F. The peaks at 454.3, 456.1, 458.5, 460.7, 462.9, and 464.5 eV for K_1P_6@Mxene correspond to Ti-C (2p3/2), Ti (III) 2p3/2, Ti-O (2p3/2), Ti (II) 2p1/2, TiC (2p1/2), and Ti-O (2p1/2), respectively [37], which are characteristic Ti2p peaks of Mxene as reported in the literature (Fig. 4G). Fig. S5A presents the high-resolution C1s spectrum for K_1P_6@Mxene. The binding energies observed at 284.7, 286.1, and 288.6 eV correspond to carbon-hydrogen (C-H) or carbon-carbon (C-C), carbon-oxygen (C-O), and carbonyl (C=O) bonds, respectively. The C-N bond at 284.9 eV originates from chitosan, while the C-Ti bond at 281.9 eV is attributed to Mxene. Nitrogen (N) is exclusively present in K_1P_6; in the N1s spectrum of K_1P_6@Mxene(Fig. S5B), two prominent peaks at approximately 400.9 eV and 399.1 eV correspond to chitosan NH_2 and CO-NH- groups. Mxene can interact with K_1P_6 through charge interactions or hydrogen bonding, further stabilising the porous framework structure. Additionally, the O1s spectrum of K_1P_6 peaked at 532.3 eV, representing C-O-C and O-H functionalities (**Fig. S5C**). Upon adding Mxene, this peak shifted to 533.4 eV, suggesting the formation of hydrogen bonds between the carboxylic acid functional groups in K_1P_6 and the hydroxyl groups in Mxene.

Biocompatibility evaluation of sponge scaffolds

Fibroblasts and endothelial cells play a crucial role in tissue healing, with their migration and proliferation being essential for wound recovery [38]. The cytotoxicity of the sponge scaffolds was evaluated using the Calcein-AM/PI double staining kit, which allowed for the visualization of live and dead cells in different extracts (Fig. 5A). At 24 h post-extract addition, both L929 cells (Fig. 5B) and HUVECs (Fig. 5D) in all groups exhibited robust growth with elongated cell morphology, showing no significant

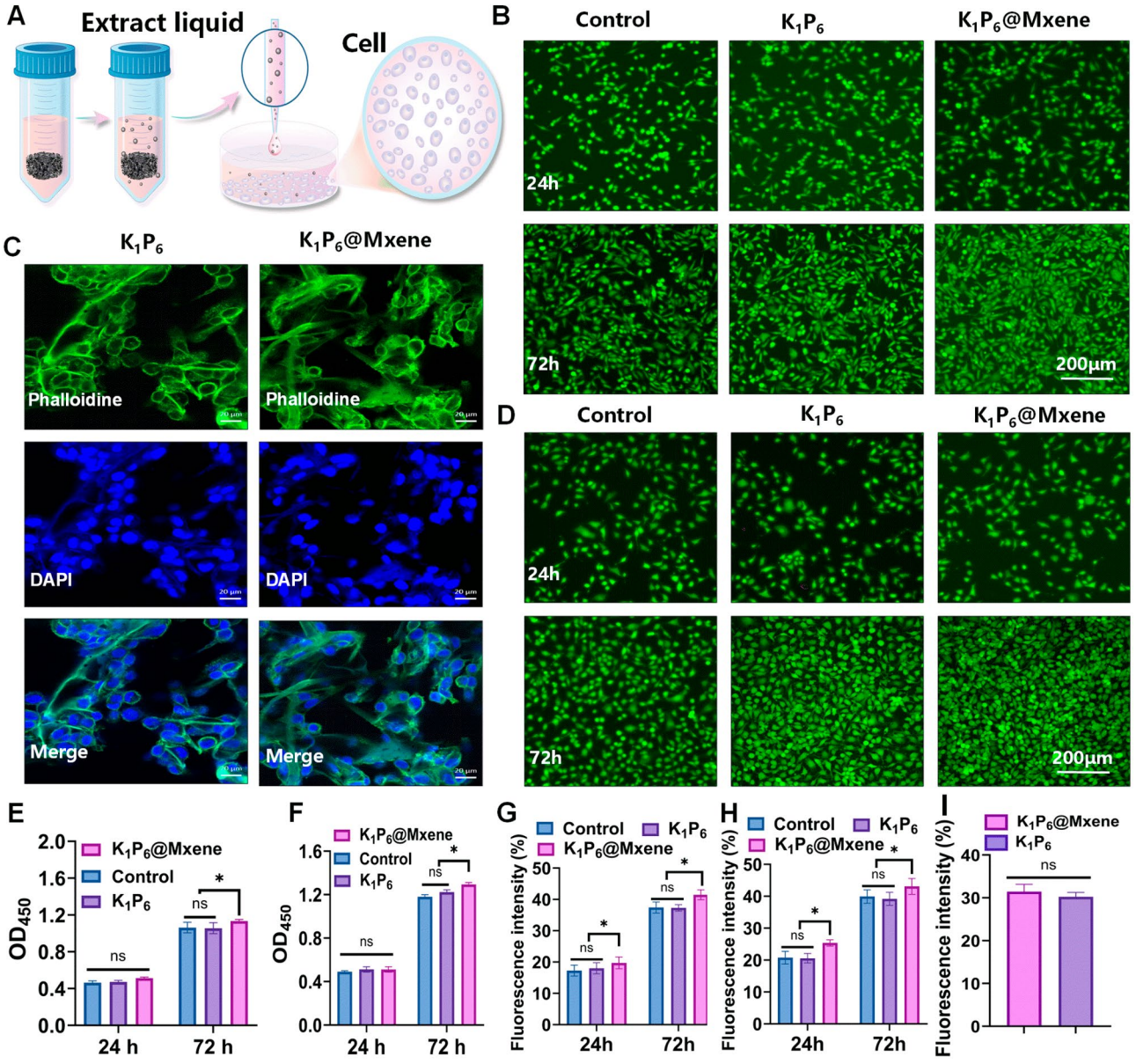

Fig. 5 Assessment of in vitro biocompatibility of sponge scaffolds. (**A**) Schematic representation of the sponge extract utilised in cell culture; (**B**) Representative images showing staining for living and dead cells of L929 cells; (**C**) Representative images demonstrating fluorescence staining of ghost-pen cyclic peptide after 3 days of co-culture with HUVECs and scaffolds; (**D**) Representative images showing staining for living and dead cells of HUVECs; (**E**) Quantitative statistical analysis from CCK-8 assay conducted on L929 cells; (**F**) Quantitative statistical analysis from CCK-8 experiments performed on HUVECs; (**G**) Quantitative analysis of green fluorescence intensity in stained HUVECs; (**H**) Quantitative analysis of green fluorescence intensity in stained L929 cells; (**I**) Quantitative immunofluorescence analysis of ghost pen cyclic peptide. The data, presented as mean ± standard deviation, were derived from three independent experiments, analysed using one-way ANOVA, followed by Tukey's post-hoc multiple comparison test (*$p < 0.05$, **$p < 0.01$, ***$p < 0.001$)

difference in cell fluorescence intensity among the groups ($p > 0.05$). After 72 h of co-culture, however, the fluorescence intensity of HUVECs (Fig. 5H) and L929 cells (Fig. 5G) in the control group was significantly weaker compared with the other two groups. In contrast, the fluorescence intensity of cells in the K_1P_6@Mxene group was notably higher than that of the K_1P_6 group ($p < 0.05$). These results confirm that K_1P_6@Mxene sponges exhibit excellent biocompatibility, as they not only lack cytotoxicity but also significantly stimulate cell proliferation.

To further assess the infiltration and adhesion capability of cells within the scaffold, HUVECs were cultured in the scaffold and subjected to fluorescent staining, as depicted in Fig. 5C. The results revealed that HUVECs could effectively infiltrated and proliferated within the scaffold, with enhanced performance observed following

Mxene modification. Quantitative immunofluorescence intensity analysis (Fig. 5I) confirmed these observations. The cytotoxicity of sponge extract was determined by CCK-8 method. The proliferative activity of L929 cells (Fig. 5E) and HUVEC cells (Fig. 5F) was evaluated by co-culturing with K_1P_6@Mxene sponge extract. After a 72 h co-culture period, OD values for all groups exhibited a general increasing trend. No statistical differences in OD values were observed among the groups at 24 h, indicating good biocompatibility across all groups. However, after 72 h of co-culture, the OD value for the K_1P_6@Mxene group significantly was significantly higher than that of the control group, suggesting that Mxene stimulation promotes the proliferation of L929 cells and HUVECs. The modified Transwell cell scratch assay was used to simulate the effect of sponge scaffolding on HUVEC migration (Fig. S6A). The dynamic migration process of endothelial cells is depicted in Fig. S6B. In the K_1P_6@Mxene group, HUVECs exhibited the fastest migration, with nearly complete contact achieved at 48 h. Additionally, at 24 h, the migration distance of HUVECs in the K_1P_6@Mxene group was significantly greater compared with the control group (Fig. S6C) ($p<0.05$). These findings indicate that Mxene doping significantly enhances cell migration in the K_1P_6@Mxene sponge, which is crucial for diabetic wound healing.

In conclusion, the K_1P_6@Mxene sponge scaffold demonstrates excellent biocompatibility and physical-chemical properties that promote the proliferation, migration, and angiogenesis of wound repair-related cells. This may be attributed to two main factors: Firstly, the K_1P_6@Mxene sponge transmits electrical signals similarly to wires, which strengthens cellular connections and communication. Secondly, the chitosan and Mxene components within K_1P_6@Mxene sponge possess anti-inflammatory and antioxidant properties, which, along with their ability to induce cell transformation, contribute to promoting cell proliferation and migration.

Evaluation of antibacterial properties of K_1P_6@Mxene

Diabetic patients often suffer from increased susceptibility to infections due to several factors, including a hyperglycaemic environment that promotes bacterial growth, a reduced immune response, diminished antibody production, and impaired white blood cell function [39]. Additionally, complications such as vascular disease and neuropathy further compromise blood and oxygen supply, facilitating bacterial invasions [40]. Therefore, the broad-spectrum antibacterial activity of wound dressings is crucial for improving the prognosis of infected wounds [41].

To evaluate the antibacterial effects of K_1P_6@Mxene, *Staphylococcus aureus* (*S. aureus*) and *Escherichia coli* (*E. coli*) were used as test organisms. As shown in Fig. 6A, after 36 h of co-culture with K_1P_6@Mxene, the sponge was found to kill 98.89% of *S. aureus* and 97.21% of *E. coli.* In contrast, the K_1P_6 sponge alone killed 70.5% of *S. aureus* and 71.9% of *E. coli*, while collagen sponges demonstrated even lower antimicrobial activity (Fig. 6C). The bacterial proliferation test further evaluated the proliferation ability of S. aureus. As shown in Fig. 6B, sponges in the K_1P_6@Mxene group showed the slowest bacterial proliferation rate, indicating excellent antibacterial activity, followed by sponges in the K_1P_6 group. The collagen sponge control group exhibited a faster bacterial proliferation rate, indicating low antibacterial activity (Fig. 6D). Similar results were observed when assessing the survival and proliferation capacity of E. coli, confirming that the K_1P_6@Mxene group possessed superior antibacterial properties compared with the other groups (Fig. 6E).

In conclusion, while the K_1P_6 sponge alone possesses some antibacterial properties, the addition of Mxene significantly enhances these properties. The proposed antibacterial mechanism is illustrated in Fig. 6F. The $-NH_2$ groups in the HPCS molecule can form $-NH_3^+$ cations in the solution by combining with free H^+. These $-NH_3^+$ ions can bind with negative anions on the bacterial cell wall through electrostatic attraction, resulting in an uneven distribution of negative charges on the cell wall and cell membrane. This disrupts the balance between natural synthesis and dissolution of the cell wall, impairing normal physiological metabolism and reproductive capability of the bacteria [42].

Furthermore, the morphology and core atomic structure of Mxenes can influence their bactericidal performance. When multilayer Mxene powder is stacked, it becomes easier to access the sharp edges, which can disrupt the bacterial cell membrane structure, thereby enhancing Mxenes' effectiveness in eradicating *E. coli* and *S. aureus*. Moreover, Mxene exhibits peroxidase-like activity, enabling it to decompose hydrogen peroxide (H_2O_2) into reactive oxygen species (ROS) that effectively eliminate bacteria. The release of low-concentration metal ions during Mxene oxidation also contributes to microbial inactivation. Additionally, the abundant hydroxyl groups on the surface of Mxene can form hydrogen bonds with bacterial cell membranes, while its surface charge can generate electrostatic forces that enhance contact with bacteria, increasing the likelihood of bacterial eradication [21, 43].

In vitro haemostatic performance evaluation of K_1P_6@Mxene

Wound healing is a complex process encompassing four main stages: haemostasis, inflammation or migration, proliferation, and tissue repair. In diabetic patients, uncontrolled bleeding and infection can significantly delay wound healing and increase the risk

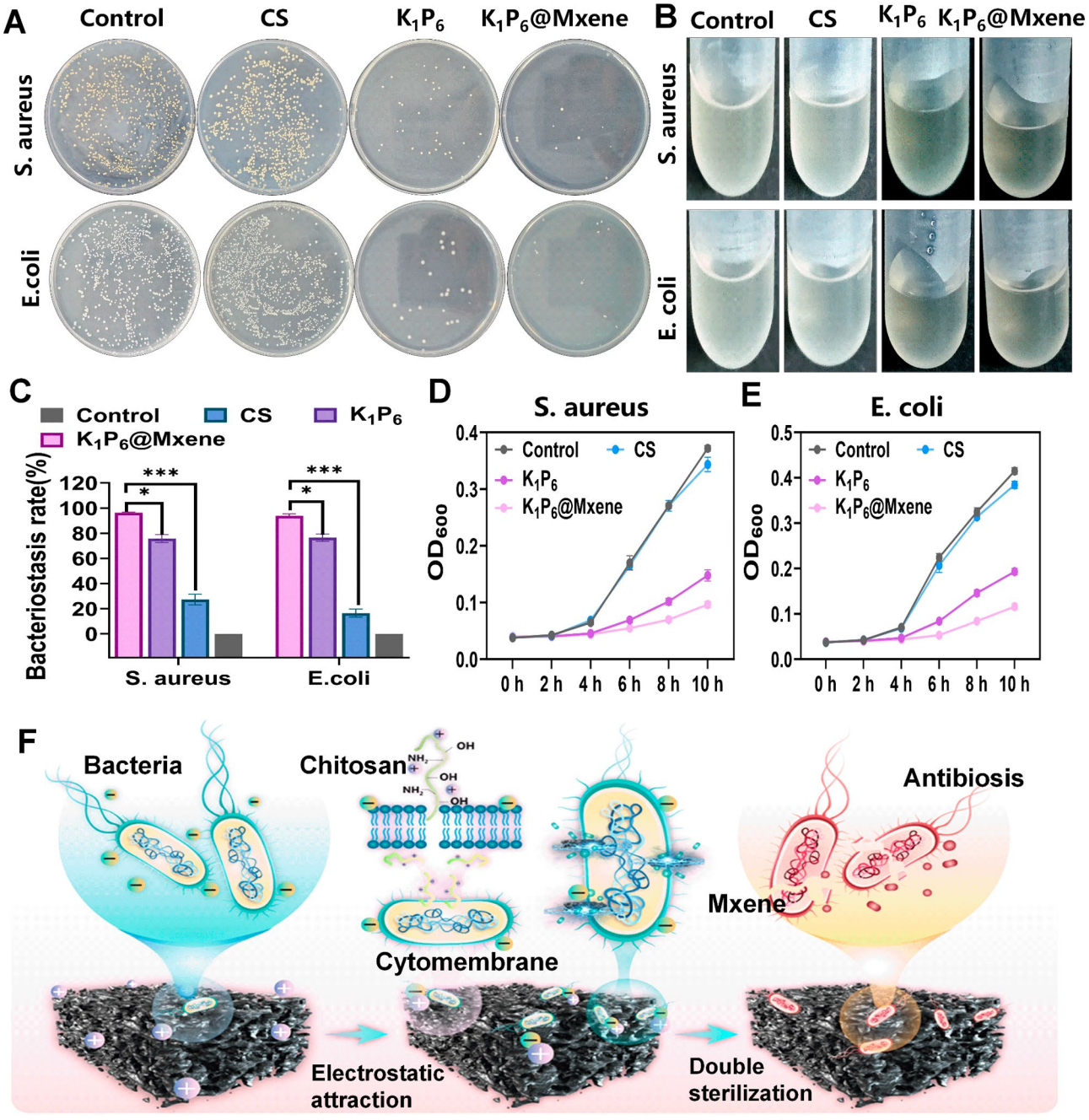

Fig. 6 Assessment of the antibacterial properties of K_1P_6@Mxene sponge scaffold. (**A**) Representative images of Staphylococcus aureus and Escherichia coli colony plates; (**B**) Representative images showing the 8-hour proliferation of Staphylococcus aureus and Escherichia coli; (**C**) Statistical analysis of Staphylococcus aureus and Escherichia coli colonies; (**D**) Proliferation curve of Staphylococcus aureus; (**E**) Growth curve of Escherichia coli; (**F**) Schematic representation of the antibacterial mechanism of K_1P_6@Mxene sponge

of trauma-related deaths. High blood glucose levels in diabetics cause excessive blood viscosity, disrupted metabolism, reduced coagulation factors, and slowed blood flow, all of which impair coagulation function [44, 45]. Although the body initiates a coagulation cascade after bleeding, severe or uncontrollable bleeding often requires external haemostatic materials [46]. Therefore, we anticipated that K_1P_6@Mxene would exhibit strong haemostatic properties.

As shown in Fig. 7A, the sponge was soaked in whole blood and cleaned with PBS after forming a blood clot. Both K_1P_6@Mxene and the commercially available collagen haemostatic sponge demonstrated effective blood cell binding. In the in vitro coagulation experiment (Fig. 7B), all sponge groups effectively promoted blood

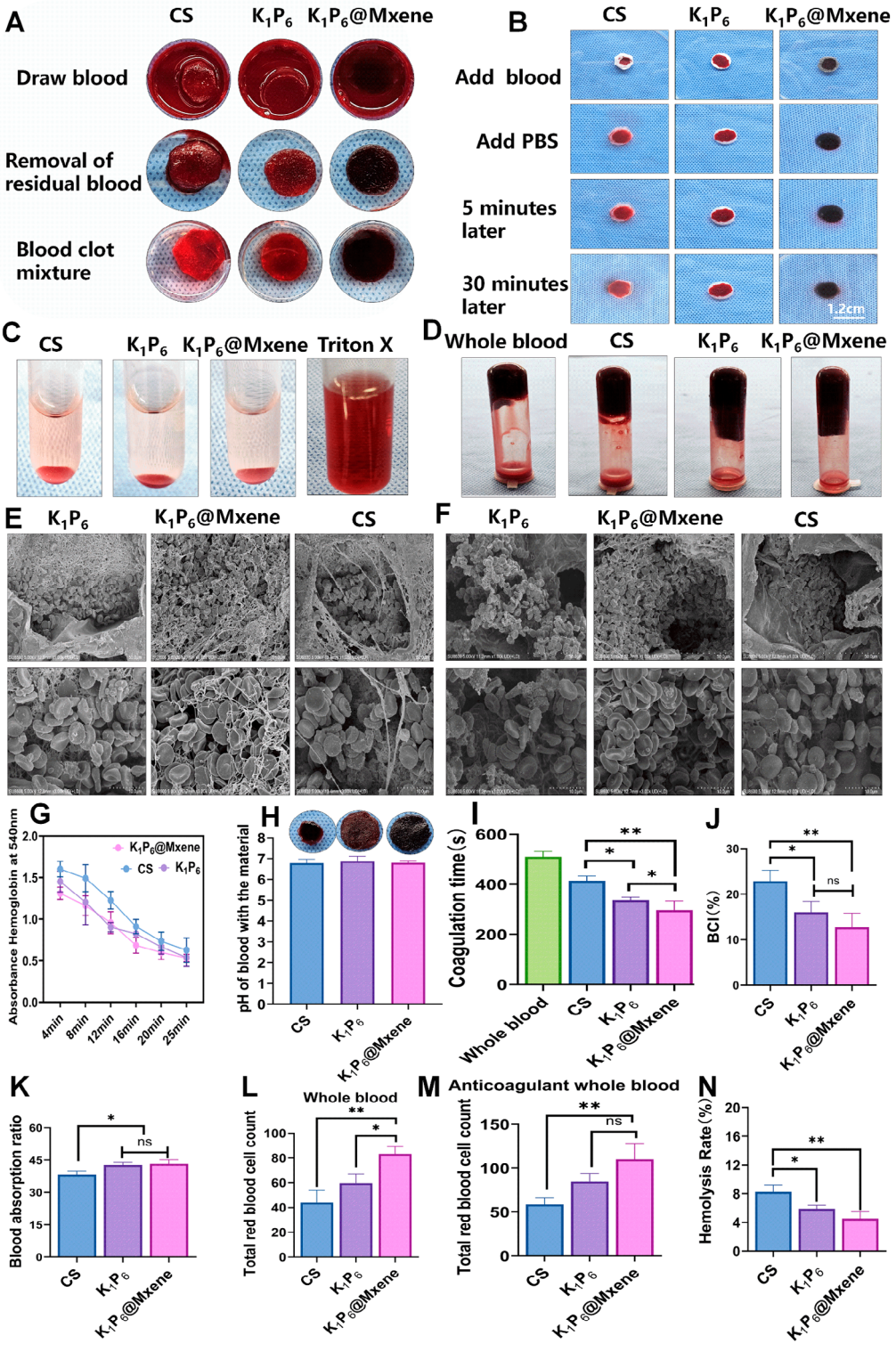

Fig. 7 In vitro haemostatic performance evaluation of K_1P_6@Mxene sponge scaffold. (**A**) Images of the sponges after blood cell adhesion; (**B**) Representative photographs of the sponges during the in vitro coagulation process; (**C**) Representative pictures of sponge haemolytic activity; (**D**) Representative pictures of sponge coagulation time measurements; (**E**) SEM images after the sponges were incubated with ordinary whole blood; (**F**) SEM images after the sponge was incubated with anticoagulated whole blood; (**G**) Whole blood coagulation dynamics; (**H**) Morphology and pH of blood clots after 24 h of immersion in PBS solution; (**I**) Coagulation time; (**J**) Blood coagulation index; (**K**) Blood absorption ratio; (**L**) Quantitative analysis of blood cells from Fig. E; (**M**) Quantitative analysis of blood cells from Fig. F; (**N**) Haemolysis rate. The data (mean ± standard deviation) were quantified from three independent experiments, one-way ANOVA, and Tukey's post-hoc multiple comparison test (*$p < 0.05$, **$p < 0.01$, ***$p < 0.001$)

clot formation. Figure 7C shows that both the K_1P_6 and K_1P_6@Mxene groups showed lower haemolysis rates compared with commercially available collagen sponges (Fig. 7N). The in vitro coagulation time (Fig. 7D) was shorter for K_1P_6 and K_1P_6@Mxene sponges than for the control group and collagen sponges, likely due to their staggered fibre structure, which enhances blood cell absorption and effusion (Fig. 7K). Notably, the K_1P_6@Mxene group exhibited a significantly shorter coagulation time compared with the CS group, indicating that the incorporation of Mxene enhances the haemostatic effectiveness of the K_1P_6 sponge (Fig. 7I).

The whole blood coagulation kinetics curve (Fig. 7G) shows that sponges in the K_1P_6@Mxene group had significantly better coagulation ability than those in the CS group ($p<0.01$). After soaking the blood clot complex in PBS and incubating at 37 ℃ for 24 h, the pH of the supernatant remained close to 7 (Fig. 7H), indicating that the sponges in each group were compatible with the physiological pH of the human body. As shown in Fig. 7J, the coagulation index in the K_1P_6@Mxene group (12±0.4)% was significantly lower than that in the CS group (22±0.5)%, with a statistically significant difference ($p<0.01$).

To better simulate the human haemostatic environment, fresh whole blood (Fig. 7E) and anticoagulant blood (Fig. 7F) were used for blood cell adhesion experiments. Microscopic morphology showed notable blood cell adhesion on the sponges in each group. Sponges in the K_1P_6@Mxene group induced a more robust fibrinogen network in fresh whole blood, allowing red blood cells and platelets to adhere more tightly. Blood count statistics further confirmed more substantial and closer clot formation on the sponges in the K_1P_6@Mxene group (Fig. 7L and M).

In summary, the K_1P_6@Mxene sponge surface exhibited significant platelet adhesion, with many platelets deforming and producing pseudopodia, indicating platelet activation. Interestingly, red blood cells exhibited two types of aggregation behaviour: some adhered to the K_1P_6@Mxene sponge surface and extended pseudopods, similar to platelet adhesion, while others became entangled with the sponge fibres, forming networks that promote haemostasis. Platelet activation and red blood cell aggregation are crucial for haemostasis. Activated platelets release adenosine diphosphate and thromboxane A2, leading to platelet embolism formation, while red blood cell accumulation aids in blood clot formation. As the main component of the K_1P_6@Mxene sponge, the porcine acellular dermal matrix can trigger platelet activation and promote the release of intracellular Ca^{2+}, accelerating thrombosis. Furthermore, haemoglobin and hydroxypropyl chitosan in the blood interact through hydrogen bonding, electrostatic forces, and van der Waals forces. Amino acid residues in haemoglobin form hydrogen bonds with hydroxyl groups in hydroxypropyl chitosan, enhancing the sponge's blood cell adsorption capacity. Additionally, negatively charged amino acid residues of haemoglobins interact electrostatically with the positive charge in hydroxypropyl chitosan, promoting platelet activation, red blood cell aggregation, morphological changes, and thrombin production [47]. The porous structure and mechanical strength of K_1P_6@Mxene enable rapid plasma absorption, concentrating platelets and red blood cells on their surface, thereby achieving rapid haemostasis.

In vivo haemostatic performance evaluation of K_1P_6@Mxene sponge scaffold

Normal haemostasis primarily relies on the intact structure and function of the blood vessel wall, sufficient high-quality platelets, and the proper functioning of coagulation factors. Negatively charged platelets and coagulation factors play particularly crucial roles. The haemostatic sponge, being fine, porous, and positively charged, can immediately adhere to and aggregate platelets upon contact with human blood, facilitating thrombosis, wound blockage, and the release of various coagulation-related factors. Through the combined actions of endogenous and exogenous coagulation pathways blood forms stable fibrin polymers, leading to the formation of blood clots and wound haemostasis [2, 48].

The haemostatic efficacy of the commercially available collagen sponge and K_1P_6@Mxene sponge was compared in a rat model of bleeding induced by tail amputation. The haemostatic process diagram is shown in Fig. 8A. While the collagen sponge alone was insufficient to absorb blood and form blood clots, the K_1P_6@Mxene sponge absorbed and immobilised the stagnant blood within its pores, successfully achieving haemostasis (Fig. 8B). Additionally, the time to achieve haemostasis (Fig. 8C) was shorter, and the amount of blood loss (Fig. 8D) was less with the K_1P_6@Mxene sponge compared with the collagen sponge alone.

The haemostatic effects of the collagen sponge and K_1P_6@Mxene sponge was also compared using a rat liver volume defect model to simulate visceral injury. The haemostatic process for the liver is depicted in Fig. 8H and I, with representative images of the haemostatic process shown in Fig. 8G. Statistical results indicated that blood loss and haemostasis time for the K_1P_6@Mxene and K_1P_6 groups were 0.17±0.02 g, 0.163±0.03 g, 82.75±4.99 s, and 81.5±5 s, respectively. In contrast, the control group had a total blood loss of 0.228±0.02 g and a haemostasis time of 106±7.53 s (Fig. 8E and F).

As previously discussed, K_1P_6 facilitates the aggregation of blood cells near the incision, rapidly concentrating the blood and activating clotting factors to halt bleeding.

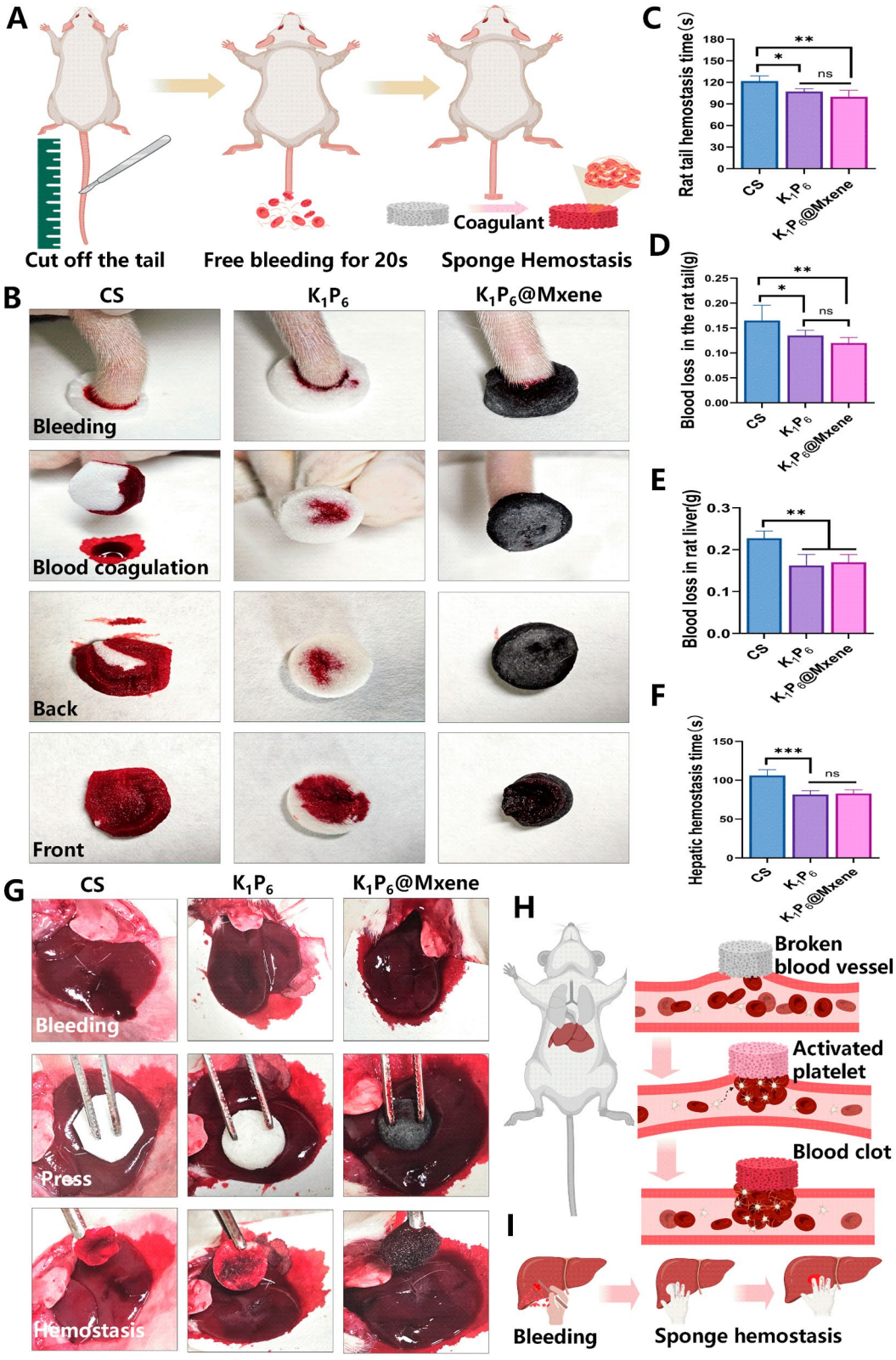

Fig. 8 K_1P_6 @Mxene sponge applied to rat tail haemorrhage and liver haemorrhage models. (**A**) Schematic diagram of rat tail amputation haemostasis experiment; (**B**) Representative images of the tail haemostasis process; (**C**) Time to achieve tail haemostasis; (**D**) Volume of blood loss from the tail; (**E**) Volume of blood loss from the liver; (**F**) Time to achieve hepatic haemostasis; (**G**) Operation processes of rat liver haemostasis experiment; (**H**) Mechanism behind rat liver haemostasis; (**I**) Schematic diagram of rat liver haemostasis. The data (mean ± standard deviation) were quantified from three independent experiments, one-way ANOVA, and Tukey's post-hoc multiple comparison test (*$p < 0.05$, **$p < 0.01$, ***$p < 0.001$)

Additionally, the hydroxyl groups in Mxene strongly chelate with the trivalent iron ions in the blood, further accelerating the haemostasis process [49, 50].

Evaluation of the ability of K_1P_6@Mxene sponge scaffold to promote diabetic wound healing

Three-dimensional scaffolds with endogenous electric field coupling are crucial for guiding cell proliferation, infiltration, and angiogenesis. These processes directly impact wound healing, including contraction, granulation tissue formation, and leukocyte infiltration [51]. This study evaluated the ability of the K_1P_6@Mxene sponge scaffold to promote wound healing in a diabetic rat model with full-thickness skin defects (Fig. 9B).

The wound healing progress of four groups of diabetic rats was monitored at 0, 3, 7, 14, 21, and 28 days after surgery (Fig. 9A). Over time, the wound areas in all treatment groups decreased to varying extents, with a notable trend in wound area reduction: Control group > CS sponge group > K_1P_6 sponge group > K_1P_6@Mxene sponge group. By day 7, the control group exhibited slow wound closure, with incomplete scabbing and minor yellow pus. In contrast, wounds in the treatment groups were completely crusted, drier, and smaller, likely due to the increased hydrophilicity of the test materials, which absorbed secretions and kept the wound dry. By day 14, the K_1P_6@Mxene sponge group exhibited an expanded wound healing area with a healing rate of 87% ± 2%, compared with 75% ± 3% in the control group and 80% ± 2% in the CS group. By day 28, the regenerated skin tissue treated with the K_1P_6@Mxene sponge showed minimal scarring (Fig. 9C), indicating that the K_1P_6@Mxene sponge effectively promotes new tissue growth while reducing scar tissue formation.

The wound healing process was further assessed for pathological features using H&E and Masson staining tests. The findings revealed a significantly reduced wound length in the K_1P_6@Mxene sponge group compared with the control and CS groups (Fig. 9D and H). Additionally, wounds in the K_1P_6@Mxene group exhibited thinner granulation tissue (Fig. 9G), enhanced and more organised collagen deposition (Fig. 9E **and** Fig. 9F), as well as a thicker epidermis at day 7 when compared with the control group. These observations indicate that the K_1P_6@Mxene sponge may promote the formation of skin appendages, thereby attenuating scar tissue regeneration during the early stages of diabetic wound healing.

Immunohistochemical analysis

The persistent and chronic inflammatory microenvironment in diabetic wounds disrupts the normal function of endogenous or transferable bioactive factors, thereby impeding wound healing [52]. Research indicates that Mxene-modified nanofiber membranes exhibit programmed antibacterial and anti-inflammatory properties, which aid in the healing of infected wounds by inhibiting the NF-kB pathway [53]. TNF-α, a pro-inflammatory cytokine secreted by macrophages, plays a role in normal inflammatory and immune responses while also regulating tissue homeostasis by co-regulating other cytokines, cell survival, and death [54]. As shown in Fig. 10A, TNF-α immunostaining results reveal that all sponge-treated wound tissues initially exhibited increased inflammatory cells and fibroblasts on day 3, with inflammation gradually subsiding by day 7. A clear trend in the TNF-α positive area was observed: Control group > CS sponge group > K_1P_6 sponge group > K_1P_6@Mxene sponge group (Fig. 10G).

IL-10, an anti-inflammatory cytokine secreted by macrophages, is a crucial regulator of immune response. It directly impacts antigen-presenting cells (APCs) by down-regulating the expression of MHC Class II and co-stimulatory molecules on the surfaces of macrophages and monocytes. The IL-10 immunostaining results shown in Fig. 10B demonstrate a robust anti-inflammatory response in all sponge-treated wound tissues by day 7. The IL-10 positive area followed a distinct trend: Control group < CS sponge group < K_1P_6 sponge group < K_1P_6@Mxene sponge group (Fig. 10F). These findings suggest that the K_1P_6@Mxene sponge possesses significant anti-inflammatory effects.

Angiogenesis is crucial for tissue repair, as it facilitates blood perfusion to the wound, delivering oxygen and nutrients that promote cell proliferation, including fibroblast proliferation. To further investigate blood vessel formation during wound healing, CD31 immunofluorescence staining was employed [55]. As depicted in Fig. 10C, strong positive expression of CD31 was observed in the K_1P_6@Mxene and K_1P_6 groups, except in the control group. Blood vessels were more widely distributed and had larger diameters, particularly in the K_1P_6@Mxene group, where statistically significant differences were noted in fluorescence quantification (Fig. 10I) ($p < 0.05$).

The two primary types of skin collagen, type I and type III, are integral to skin damage repair. Figure 10D shows that type I collagen deposition increased over time across all groups, with a significant rise in the K_1P_6@Mxene group (Fig. 10H) ($p < 0.05$). Previous research has demonstrated that adequate type I collagen supplementation during the later stages of wound healing significantly aids remodelling and reduces scar formation. Upon complete wound healing, the process enters the stage of scar hyperplasia, where α-SMA immunofluorescence staining can be used to assess scar formation in diabetic wound healing in vivo. As depicted in Fig. 10E, α-SMA positive expression decreased to varying degrees on days 21 and 28 across all groups, with wounds treated with K_1P_6@

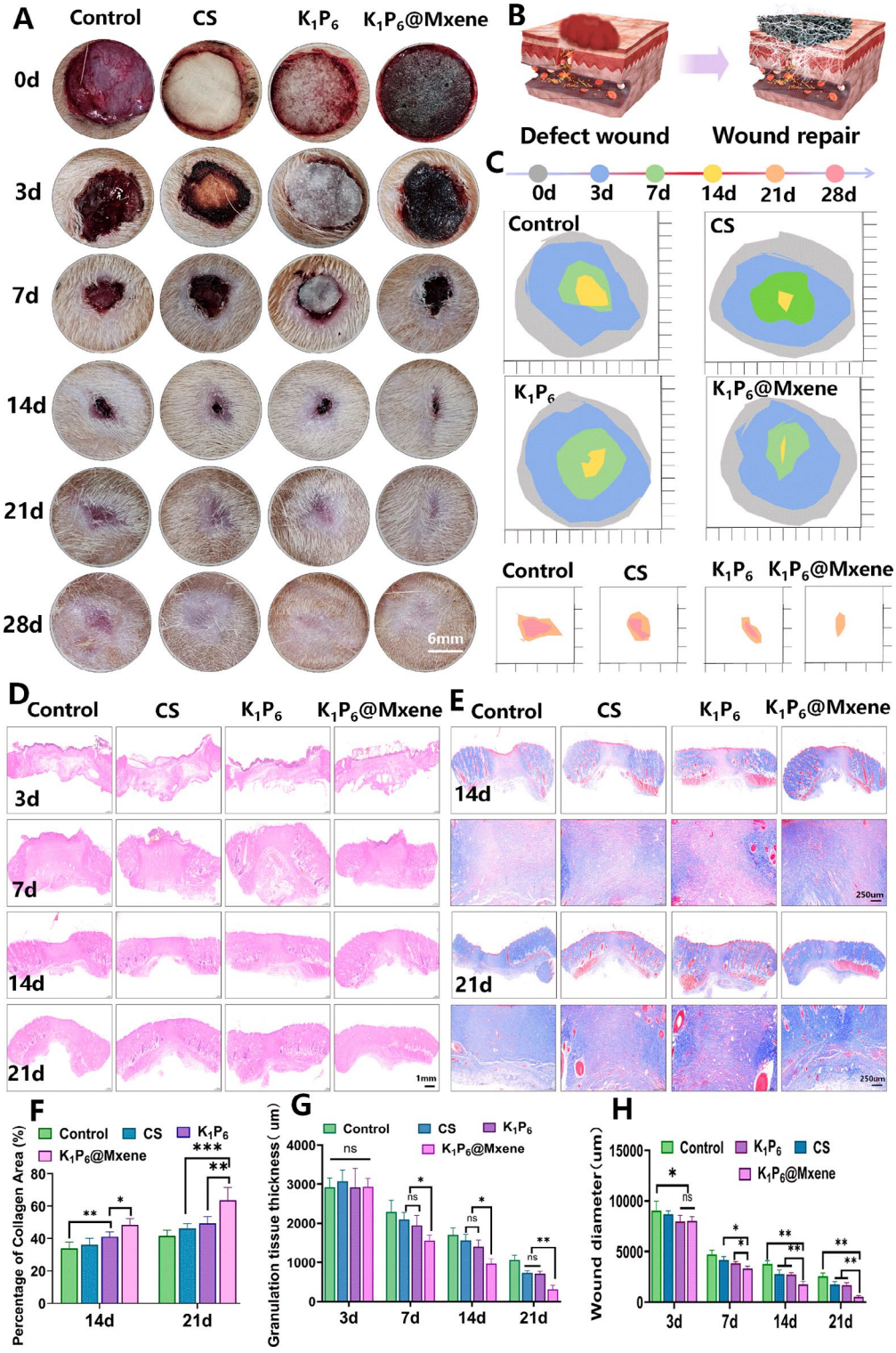

Fig. 9 Evaluation of K_1P_6 @Mxene sponge in treating diabetic wounds in rats. (**A**) Dynamic wound healing and scarring processes captured at different time points in each treatment group; (**B**) Schematic diagram of accelerated wound closure with sponge scaffold; (**C**) Dynamic wound healing and scar formation observed in each treatment group at various time points; (**D**) H&E staining images depicting the histological changes in each treatment group over time; (**E**) Masson staining images of each treatment group at various time points; (**F**) Quantitative analysis of Masson staining results; (**G**) Quantitative analysis of granulation tissue thickness; (**H**) Quantitative analysis of wound diameter. The data (mean ± standard deviation) were obtained from three independent experiments and analysed using one-way ANOVA, followed by Tukey's post-hoc multiple comparison test (*$p < 0.05$, **$p < 0.01$, ***$p < 0.001$)

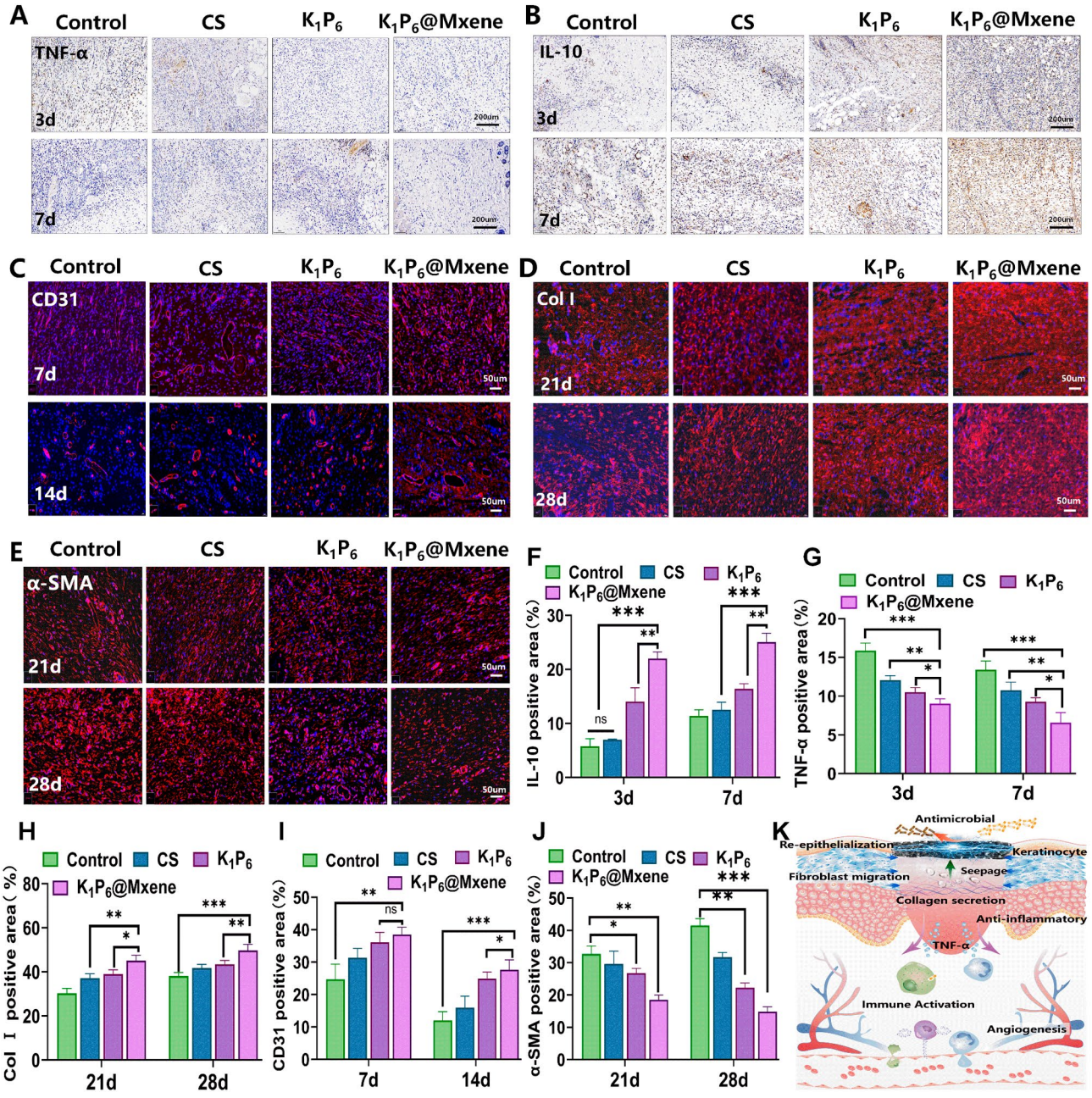

Fig. 10 Immunohistological analysis. (**A**) Representative TNF-α immunohistochemical staining images of each group on day 3 and day 7; (**B**) Representative IL-10 immunohistochemical staining images of each group on day 3 and day 7; (**C**) Each group was stained with CD31 immunofluorescence on day 7 and day 14; (**D**) Fluorescent staining representative images of type I collagen of different treatment groups at day 21 and day 28; (**E**) α-SMA immunofluorescence staining of different treatment groups at day 21 and day 28; (**F**) Quantification of IL-10 positive area in each group; (**G**) Quantification of TNF-α positive area in each group; (**H**) Quantification of the relative positive area of type I collagen; (**I**) Quantification of the relative positive area of CD31; (**J**) Quantification of α-SMA immunofluorescence density in each group; (**K**) K_1P_6@Mxene Schematic diagram of a possible mechanism by which sponges accelerate diabetic wound healing. The data (mean ± standard deviation) were quantified by three independent experiments, one-way ANOVA, and Tukey's post-hoc multiple comparison test (*$p < 0.05$, **$p < 0.01$, ***$p < 0.001$)

Mxene showing significantly low levels ($p < 0.05$), as confirmed by fluorescence quantification (Fig. 10J).

These findings suggest that K_1P_6@Mxene treatment reduces inflammatory response during the wound stage, promotes angiogenesis in the intermediate phase, enhances collagen deposition and remodelling in the late stage, and helps prevent scar formation in healed tissue. This effect may be attributed to the electrically active nature of the K_1P_6@Mxene sponge scaffold, which leverages endogenous electric fields to augment

the recruitment of immune cells and cytokines at the site of injury, thereby reducing pro-inflammatory cytokine expression levels and shortening the inflammatory period. Furthermore, during the cell proliferation stage, various cells involved in wound healing, such as endothelial cells, fibroblasts, and epithelial cells, respond to endogenous electrical signals. Guided by these signals, fibroblasts proliferate and secrete collagen to facilitate granulation tissue formation, while endothelial cells accelerate migration and vascularisation. Additionally, PADM exhibits composition and properties closely resembling those of the human extracellular matrix (ECM), making it an ideal substitute for simulating the ECM microenvironment. It provides chemical and mechanical cues for cellular activities, including adhesion and proliferation, thereby promoting tissue repair and regeneration [21].

K_1P_6@Mxene: potential mechanism of sponges for diabetic wound repair

The wound repair process involves a complex sequence of cellular and biochemical events across four stages: haemostasis, inflammation, proliferation, and tissue remodelling. Diabetic wound repair often encounters challenges during the haemostasis and inflammation stages due to inadequate management of wound fluids and the failure to actively harness endogenous electric fields. This results in passive tissue repair, negatively impacting the overall cascade of tissue regeneration.

Mxene exhibits excellent electrical conductivity, and its incorporation into the K_1P_6 system enhances the electrical activity of the K_1P_6@Mxene sponge. The scaffold's high water absorption and moisturising capabilities enable it to effectively manage exudate from diabetic wounds while serving as a conduit for transmitting interrupted bioelectrical signals. This active transmission facilitates precise tissue remodelling within the tissue repair cascade.The outstanding performance of K_1P_6@Mxene in tissue repair can be attributed to several mechanisms: (1) Mimicking the extracellular matrix: The fibrous structure of K_1P_6 resembles the natural extracellular matrix, with high porosity and specific surface area, creating an optimal environment for cell adhesion, oxygen exchange, and skin cell growth. Additionally, hydroxypropyl chitosan promotes fibroblast migration, collagen deposition, and orderly fibre arrangement, supporting structural remodelling and tissue construction. (2) Enhanced affinity and antibacterial properties: Incorporating PADM and hydroxypropyl chitosan into the K_1P_6@Mxene scaffold improves its affinity for cells and tissues, enhancing adhesion to defective tissue sites. The addition of Mxene also boosts the scaffold's antibacterial activity and electrical conductivity, offering an effective strategy for managing wound bacterial infections. (3) Moisture management and mechanical stability: The stent's three-dimensional porous structure and exceptional mechanical stability enable reversible water absorption, effectively managing wound exudate during healing and haemostasis. This maintains a moist wound environment, reduces the risk of infection, and promotes optimal healing conditions. (4) Transmission of bioelectricity: Upon absorbing wound exudate, K_1P_6@Mxene actively couples with the endogenous electric field to transmit bioelectricity to the wound site. This guides cell migration and growth, enhances collagen deposition and arrangement, promotes epithelial cell growth, and inhibits excessive fibroblast proliferation, thereby reducing scar formation. (5) Tissue remodelling and macrophage differentiation: During tissue remodelling, K_1P_6@Mxene sponge scaffolds have demonstrated an ability to attract and differentiate macrophages through exposure to endogenous electric fields. They also generate bioactive factors that facilitate diabetic wound healing by reducing inflammation, promoting microvascular regeneration, and improving blood circulation. This delivers essential nutrients for cellular growth, enhances cell proliferation, increases cytokeratin expression, and ultimately facilitates tissue reepithelialisation. This coordinated cascade aligns with the intricate in vivo tissue damage remodelling process (Fig. 10K).

However, certain limitations exist in this study, such as focusing on demonstrating biological material applications without delving into the associated molecular mechanisms and not deeply investigating how endogenous electric fields influence cellular behaviour. Our team plans to address these gaps by further exploring the mechanisms through which endogenous and exogenous electric fields impact diabetic wound healing.

Conclusion

In this study, we have innovatively prepared a K_1P_6@Mxene sponge with exceptional physical, chemical, and electrical properties by combining physical homogeneous dispersion and chemical modification. Specifically, acellular dermal matrix fibres and water-soluble chitosan molecular interpenetrating network structure are formed through covalent cross-linking, creating a micro negative pressure on the wound surface that actively promotes exudate and blood absorption. The unique Mxene modification enhances the sponge's ability to couple with the endogenous electric field, significantly boosting the antibacterial action of the K_1P_6 sponge. Furthermore, the K_1P_6@Mxene sponge actively couples with the endogenous electric field and transmits endogenous bioelectricity to the wound surface after absorbing wound exudate, guiding cell migration and growth while influencing tissue cascade repair processes. In diabetic wound models, the K_1P_6@Mxene sponge has been shown to reduce early

inflammatory reactions, promote angiogenesis and collagen deposition, and minimise scar formation, thereby improving speed and quality of healing in diabetic patients following skin damage. With its haemostatic, anti-inflammatory, and antibacterial functions, this sponge offers a novel approach for comprehensive repair in diabetic patients, preventing acute diabetic wounds from developing into chronic refractory conditions.

Abbreviations

ECM	Extracellular matrix
PADM	Porcine acellular dermal matrix
CS	Collagen sponge
EF	Electric fields
FTIR	4′,6-diamidino-2-phenylindole
HF	Hydrofluoric acid
SEM	Scanning electron microscopy
TEM	Transmission electron microscope
DMEM	Dulbecco's Modified Eagle Medium
CFU	Colony forming units
HUVECs	Human umbilical vein endothelial cells
SD	Sprague-Dawley
H&E	Haematoxylin and eosin
Masson	Masson's trichrome stain
α-SMA	Alpha-Smooth Muscle Actin
CD31	Platelet Endothelial Cell Adhesion Molecule-1
Ki67	Marker of Proliferation Ki-67
CK14	Cytokeratin 14

Supplementary Information

The online version contains supplementary material available at https://doi.org/10.1186/s12951-024-02799-5.

Supplementary Material 1

Author contributions

H Z, LL C: Writing–original draft, Methodology, Investigation, Formal analysis, Data curation, Conceptualization. CY H: Writing–original draft, Visualization, Methodology, Investigation, Data curation. ZW J， HH Z: Supervision, Methodology, Investigation. XY L, FY Z, QL W: Methodology, Investigation. PW S, Kun L, L Y: Writing—review and editing, Supervision, Project administration, Funding acquisition.

Funding

This work was financially supported by the National Natural Science Foundation of China [No. 82372526, No. 82302797], Guangdong Basic and Applied Basic Research Foundation [No. 2023A1515012970, No. 2020A1515010107, No.2023A1515012726], The Science and Technology Innovation Project of Guangdong Province [No. 2018KJYZ005], Guangzhou Basic and Applied Basic Research Foundation (No. 2023A04J2268), Guangdong Medical Research Fund Project [A2024389], Research Foundation of YunFu People's Hospital [A20231001], Yunfu Medical and Health Research Project [2022B004]. The authors would like to acknowledge those who contributed to this article.

Data availability

All data generated or analysed during this study are included in this article.

Declarations

Ethics approval and consent to participate

The animal ethics committee approved all animal experiment studies of Nanfang Hospital of Southern Medical College (R202308.22, Guangzhou, China) and conducted by the National Research Council Guide for the Care and Use of Laboratory Animals.

Consent for publication

All authors are Consent for publication.

Competing interests

The authors declare no competing interests.

Received: 16 July 2024 / Accepted: 22 August 2024
Published online: 02 September 2024

References

1. Rodrigues M, Kosaric N, Bonham CA, Gurtner GC. Wound Healing: a Cellular Perspective. Physiol Rev. 2019;99(1):665–706. https://doi.org/10.1152/physrev.00067.2017.
2. Guo B, Dong R, Liang Y, Li M. Haemostatic materials for wound healing applications, Nature reviews. Chemistry. 2021;5(11):773–91. https://doi.org/10.1038/s41570-021-00323-z.
3. Mirhaj M, Varshosaz J, Labbaf S, Emadi R, Seifalian AM, Sharifianjazi F, Tavakoli M. Mupirocin loaded core-shell pluronic-pectin-keratin nanofibers improve human keratinocytes behavior, angiogenic activity and wound healing. Int J Biol Macromol. 2023;253:126700.
4. Mirhaj M, Varshosaz J, Labbaf S, Emadi R, Seifalian AM, Sharifianjazi F. An antibacterial multi-layered scaffold fabricated by 3D printing and electrospinning methodologies for skin tissue regeneration. Int J Pharm. 2023;645:123357.
5. Mohamed SA, Hargest R. Surgical anatomy of the skin. Surg (Oxford). 2022;40(1):1–7.
6. Esmaeili Y, Bidram E, Bigham A, Atari M, Azadani RN, Tavakoli M, Salehi S, Mirhaj M, Basiri A, Mirzavandi Z. Exploring the evolution of tissue engineering strategies over the past decade: from cell-based strategies to gene-activated matrix. Alexandria Eng J. 2023;81:137–69.
7. Dixon D, Edmonds M. Managing Diabetic Foot Ulcers: Pharmacotherapy for Wound Healing. Drugs. 2021;81(1):29–56. https://doi.org/10.1007/s40265-020-01415-8.
8. Freedman BR, Hwang C, Talbot S, Hibler B, Matoori S, Mooney DJ. Breakthrough treatments for accelerated wound healing. Sci Adv. 2023;9(20):eade7007. https://doi.org/10.1126/sciadv.ade7007.
9. Serbis A, Giapros V, Kotanidou EP, Galli-Tsinopoulou A, Siomou E. Diagnosis, treatment and prevention of type 2 diabetes mellitus in children and adolescents. World J Diabetes. 2021;12(4):344–65. https://doi.org/10.4239/wjd.v12.i4.344.
10. Wang J, Lin J, Chen L, Deng L, Cui W. Endogenous Electric-Field-coupled Electrospun Short Fiber via Collecting Wound Exudation, Advanced materials (Deerfield Beach. Fla). 2022;34(9):e2108325. https://doi.org/10.1002/adma.202108325.
11. McCaig CD, Rajnicek AM, Song B, Zhao M. Controlling cell behavior electrically: current views and future potential, Physiological reviews (2005).
12. Guo A, Song B, Reid B, Gu Y, Forrester JV, Jahoda CA, Zhao M. Effects of physiological electric fields on migration of human dermal fibroblasts. J Invest Dermatol. 2010;130(9):2320–7. https://doi.org/10.1038/jid.2010.96.
13. Tai G, Tai M, Zhao M. Electrically stimulated cell migration and its contribution to wound healing. Burns Trauma. 2018;6:20. https://doi.org/10.1186/s41038-018-0123-2.
14. Luo R, Dai J, Zhang J, Li Z. Accelerated skin Wound Healing by Electrical Stimulation. Adv Healthc Mater. 2021;10(16):e2100557. https://doi.org/10.1002/adhm.202100557.
15. Tan MLL, Chin JS, Madden L, Becker DL. Challenges faced in developing an ideal chronic wound model. Expert Opin Drug Discov. 2023;18(1):99–114. https://doi.org/10.1080/17460441.2023.2158809.
16. Tacconelli E, Carrara E, Savoldi A, Harbarth S, Mendelson M, Monnet DL, Pulcini C, Kahlmeter G, Kluytmans J, Carmeli Y, Ouellette M, Outterson K, Patel J, Cavaleri M, Cox EM, Houchens CR, Grayson ML, Hansen P, Singh N, Theuretzbacher U, Magrini N. Discovery, research, and development of new antibiotics: the WHO priority list of antibiotic-resistant bacteria and tuberculosis, the Lancet. Infect Dis. 2018;18(3):318–27. https://doi.org/10.1016/s1473-3099(17)30753-3.
17. Hameed S, Sharif S, Ovais M, Xiong H. Emerging trends and future challenges of advanced 2D nanomaterials for combating bacterial resistance. Bioactive Mater. 2024;38:225–57.
18. Ma J, Zhang L, Lei B. Multifunctional MXene-Based bioactive materials for Integrated Regeneration Therapy. ACS Nano. 2023;17(20):19526–49. https://doi.org/10.1021/acsnano.3c01913.

19. Yu Y, Sun H, Lu Q, Sun J, Zhang P, Zeng L, Vasilev K, Zhao Y, Chen Y, Liu P. Spontaneous formation of MXene-oxidized sono/chemo-dynamic sonosensitizer/nanocatalyst for antibacteria and bone-tissue regeneration. J Nanobiotechnol. 2023;21(1):193. https://doi.org/10.1186/s12951-023-01933-z.
20. Yang C, Luo Y, Lin H, Ge M, Shi J, Zhang X. Niobium carbide MXene augmented medical implant elicits bacterial infection elimination and tissue regeneration. ACS Nano. 2020;15(1):1086–99.
21. Li Y, Fu R, Duan Z, Zhu C, Fan D. Artificial Nonenzymatic antioxidant MXene Nanosheet-Anchored Injectable Hydrogel as a mild photothermal-controlled oxygen release platform for Diabetic Wound Healing. ACS Nano. 2022;16(5):7486–502. https://doi.org/10.1021/acsnano.1c10575.
22. Tavakoli M, Mirhaj M, Varshosaz J, Al-Musawi MH, Almajidi YQ, Danesh Pajooh AM, Shahriari-Khalaji M, Sharifianjazi F, Alizadeh M, Labbaf S. Keratin-and VEGF-Incorporated Honey-based sponge–nanofiber dressing: an Ideal Construct for Wound Healing. ACS Appl Mater Interfaces. 2023;15(48):55276–86.
23. Zhang H, Wang Y, Zheng Z, Wei X, Chen L, Wu Y, Huang W, Yang L. Strategies for improving the 3D printability of decellularized extracellular matrix bioink. Theranostics. 2023;13(8):2562.
24. Chen L, Huang C, Zhong Y, Chen Y, Zhang H, Zheng Z, Jiang Z, Wei X, Peng Y, Huang L. Multifunctional sponge scaffold loaded with concentrated growth factors for promoting wound healing. Iscience 26(1) (2023).
25. Chen L, Ma J, Chen Y, Huang C, Zheng Z, Gao Y, Jiang Z, Wei X, Peng Y, Yu S. Polydopamine modified acellular dermal matrix sponge scaffold loaded with a-FGF: promoting wound healing of autologous skin grafts. Biomaterials Adv. 2022;136:212790.
26. Chen S, Li A, Wang Y, Zhang Y, Liu X, Ye Z, Gao S, Xu H, Deng L, Dong A, Zhang J. Janus polyurethane sponge as an antibiofouling, antibacterial, and exudate-managing dressing for accelerated wound healing. Acta Biomater. 2023;171:428–39. https://doi.org/10.1016/j.actbio.2023.09.015.
27. Jawaid A, Hassan A, Neher G, Nepal D, Pachter R, Kennedy WJ, Ramakrishnan S, Vaia RA. Halogen Etch of Ti(3)AlC(2) MAX Phase for MXene Fabrication. ACS Nano. 2021;15(2):2771–7. https://doi.org/10.1021/acsnano.0c08630.
28. Vachhrajani V, Khakhkhar P. Science of wound healing and dressing materials. Springer; 2020.
29. Huang X, Fu Q, Deng Y, Wang F, Xia B, Chen Z, Chen G. Surface roughness of silk fibroin/alginate microspheres for rapid hemostasis in vitro and in vivo. Carbohydr Polym. 2021;253:117256. https://doi.org/10.1016/j.carbpol.2020.117256.
30. Zhu B, Wang K, Gao H, Wang Q, Pan X, Fan M. Functional Group Modification and Bonding characteristics of Ti3C2 MXene-Organic composites from First-principles calculations. ChemPhysChem. 2021;22(16):1675–83.
31. Peng S, Jin G, Li L, Li K, Srinivasan M, Ramakrishna S, Chen J. Multi-functional electrospun nanofibres for advances in tissue regeneration, energy conversion & storage, and water treatment. Chem Soc Rev. 2016;45(5):1225–41. https://doi.org/10.1039/c5cs00777a.
32. Wang Y, Wang H, Lu B, Yu K, Xie R, Lan G, Xie J, Hu E, Lu F. A sandwich-like silk fibroin/polysaccharide composite dressing with continual biofluid draining for wound exudate management. Int J Biol Macromol. 2023;253(Pt 4):127000. https://doi.org/10.1016/j.ijbiomac.2023.127000.
33. Migneault I, Dartiguenave C, Bertrand MJ, Waldron KC. Glutaraldehyde: behavior in aqueous solution, reaction with proteins, and application to enzyme crosslinking. Biotechniques. 2004;37(5):790–802.
34. Bae S, Espinosa-García W, Kang YG, Egawa N, Lee J, Kuwahata K, Khazaei M, Ohno K, Kim YH, Han MJ. MXene Phase with C3 structure unit: a family of 2D electrides. Adv Funct Mater. 2021;31(24):2100009.
35. Moseson DE, Jordan MA, Shah DD, Corum ID, Alvarenga BR Jr., Taylor LS. Application and limitations of thermogravimetric analysis to delineate the hot melt extrusion chemical stability processing window. Int J Pharm. 2020;590:119916. https://doi.org/10.1016/j.ijpharm.2020.119916.
36. Petrova OV, Sivkov DV, Nekipelov SV, Vinogradov AS, Korusenko PM, Isaenko SI, Skandakov RN, Bakina KA, Sivkov VN. Study of Marine sponges Graphitization during Heat Treatment up to 1200° C. Appl Sci. 2022;13(1):128.
37. Natu V, Benchakar M, Canaff C, Habrioux A, Celerier S, Barsoum MW. A critical analysis of the X-ray photoelectron spectra of Ti3C2Tz MXenes. Matter. 2021;4(4):1224–51.
38. Talbott HE, Mascharak S, Griffin M, Wan DC, Longaker MT. Wound healing, fibroblast heterogeneity, and fibrosis. Cell Stem Cell. 2022;29(8):1161–80. https://doi.org/10.1016/j.stem.2022.07.006.
39. Patel B, Priefer R. Infections associated with diabetic-care devices. Diabetes Metabolic Syndrome. 2021;15(2):519–24. https://doi.org/10.1016/j.dsx.2021.02.023.
40. Holt RIG, Cockram CS, Ma RCW, Luk AOY. Diabetes and infection: review of the epidemiology, mechanisms and principles of treatment. Diabetologia. 2024;67(7):1168–80. https://doi.org/10.1007/s00125-024-06102-x.
41. Liang Y, He J, Guo B. Functional hydrogels as Wound Dressing to Enhance Wound Healing. ACS Nano. 2021;15(8):12687–722. https://doi.org/10.1021/acsnano.1c04206.
42. Mohammed AM, Hassan KT, Hassan OM. Assessment of antimicrobial activity of chitosan/silver nanoparticles hydrogel and cryogel microspheres. Int J Biol Macromol. 2023;233:123580. https://doi.org/10.1016/j.ijbiomac.2023.123580.
43. Zhang WJ, Li S, Yan YZ, Park SS, Mohan A, Chung I, Ahn SK, Kim JR, Ha CS. Dual (pH- and ROS-) responsive antibacterial MXene-Based Nanocarrier for Drug Delivery. Int J Mol Sci. 2022;23(23). https://doi.org/10.3390/ijms232314925.
44. Shearer AM, Wang Y, Fletcher EK, Rana R, Michael ES, Nguyen N, Abdelmalek MF, Covic L, Kuliopulos A. PAR2 promotes impaired glucose uptake and insulin resistance in NAFLD through GLUT2 and akt interference, Hepatology (Baltimore. Md). 2022;76(6):1778–93. https://doi.org/10.1002/hep.32589.
45. Zhu W, Guo S, Homilius M, Nsubuga C, Wright SH, Quan D, Kc A, Eddy SS, Victorio RA, Beerens M, Flaumenhaft R, Deo RC, MacRae CA. PIEZO1 mediates a mechanothrombotic pathway in diabetes. Sci Transl Med. 2022;14(626):eabk1707. https://doi.org/10.1126/scitranslmed.abk1707.
46. Hickman DA, Pawlowski CL, Sekhon UD, Marks J, Gupta AS. Biomaterials and advanced technologies for hemostatic management of bleeding. Adv Mater. 2018;30(4):1700859.
47. Sun B, Zhang P, Zhang J, Huang T, Li C, Yang W. Preparation, characterization and bioavailability studies of Tegillarca granosa hemoglobin and its glycosylated products. Int J Biol Macromol. 2022;219:11–20. https://doi.org/10.1016/j.ijbiomac.2022.07.234.
48. Yan RR, Xue D, Su C, Xu Y, Gong JS, Liu YL, Jiang M, Geng Y, Lv GZ, Xu ZH, Shi JS, Biointerfaces. 218 (2022) 112770. https://doi.org/10.1016/j.colsurfb.2022.112770
49. Wu Z, Li S, Qin X, Zheng L, Fang J, Wei L, Xu C, Li ZA, Wang X. Facile preparation of fatigue-resistant mxene-reinforced chitosan cryogel for accelerated hemostasis and wound healing. Carbohydr Polym. 2024;334:121934. https://doi.org/10.1016/j.carbpol.2024.121934.
50. Li S, Gu B, Li X, Tang S, Zheng L, Ruiz-Hitzky E, Sun Z, Xu C, Wang X. MXene-Enhanced chitin composite sponges with antibacterial and hemostatic activity for Wound Healing. Adv Healthc Mater. 2022;11(12):e2102367. https://doi.org/10.1002/adhm.202102367.
51. Cheah YJ, Buyong MR, Mohd MH, Yunus. Wound healing with electrical stimulation technologies: a review. Polymers. 2021;13(21):3790.
52. Raziyeva K, Kim Y, Zharkinbekov Z, Kassymbek K, Jimi S, Saparov A. Immunology of acute and chronic wound healing. Biomolecules. 2021;11(5):700.
53. Huang Y, He S, Yu S, Johnson HM, Chan YK, Jiao Z, Wang S, Wu Z, Deng Y. MXene-Decorated Nanofibrous membrane with programmed antibacterial and anti-inflammatory effects via steering NF-κB pathway for infectious cutaneous regeneration. Small. 2024;20(4):e2304119. https://doi.org/10.1002/smll.202304119.
54. Yang L, Wang H, Yang X, Wu Q, An P, Jin X, Liu W, Huang X, Li Y, Yan S, Shen S, Liang T, Min J, Wang F. Auranofin mitigates systemic iron overload and induces ferroptosis via distinct mechanisms. Signal Transduct Target Therapy. 2020;5(1):138. https://doi.org/10.1038/s41392-020-00253-0.
55. An R, Zhang Y, Qiao Y, Song L, Wang H, Dong X. Adipose stem cells isolated from diabetic mice improve cutaneous wound healing in streptozotocin-induced diabetic mice. Stem Cell Res Ther. 2020;11(1):120. https://doi.org/10.1186/s13287-020-01621-x.

Publisher's note